Final Technical Report (FTR)

Cover Page

a. *Federal Agency*	Department of Energy	
b. *Award Number*	DE-EE0008552	
c. *Project Title*	Diagnosing and overcoming recombination and resistive losses in non-silicon solar cells using a silicon-inspired characterization platform	
d. *Recipient Organization*	Arizona State University	
e. *Project Period*	*Start:* 01/01/2019	*End:* 07/30/2022
f. *Principal Investigator (PI)*	Zachary Holman Associate Professor zachary.holman@asu.edu (480) 965-9959	
g. *Business Contact (BC)*	Lisa Mosley Executive Director asu.awards@asu.edu (480) 727-9754	
h. *Certifying Official (if different from the PI or BC)*	Name Title Email address Phone number	

Signature of Certifying Official

02/07/2024
Date

By signing this report, I certify to the best of my knowledge and belief that the report is true, complete, and accurate. I am aware that any false, fictitious, or fraudulent information, misrepresentations, half-truths, or the omission of any material fact, may subject me to criminal, civil or administrative penalties for fraud, false statements, false claims or otherwise. (U.S. Code Title 18, Section 1001, Section 287 and Title 31, Sections 3729-3730). I further understand and agree that the information contained in this report are material to Federal agency's funding decisions and I have any ongoing responsibility to promptly update the report within the time frames stated in the terms and conditions of the above referenced Award, to ensure that my responses remain accurate and complete.

Acknowledgement: "This material is based upon work supported by the U.S. Department of Energy's Office of Energy Efficiency and Renewable Energy (EERE) under the Solar Energy Technology Office (SETO) FY2018 Funding Opportunity Announcement Award Number DE-EE0008552."

Executive Summary: This project aimed to generate the characterization tools needed for accurate and systematic loss analysis in non-silicon photovoltaic solar cell technologies and, through the use of these tools and analysis techniques, contribute to the development of a novel class of hetero-contacts to II-VI absorbers, with the final goal of demonstrating record-breaking CdSeTe devices.

CdSeTe solar cells provide a prime example of the potential impact of the techniques we proposed to develop and implement: record poly-CdSeTe cells have bandgap-voltage deficits (W_{oc}) of approximately 550 mV, as compared with below 400 mV for all other mature PV technologies. Similarly, these record CdSeTe devices have FFs below 80%, when other mature cells are near or above 85%. Frustratingly, a systematic identification of the origin of these sub-par performances—for example recombination or resistive losses—has been lacking, thus slowing down the development of these technologies. Similarly, it is often asserted that CdSeTe cells need a better back (hole) contact. Although most believe this is true, no one knew—at the start of this project—how high the V_{oc} and FF *could* be for a given cell if it had a perfect back contact.

Such characterization techniques and loss analysis methods exist and are routinely performed on c-Si solar cells (e.g. injection-dependent lifetime, Suns-V_{oc}, transfer length method, etc). Over the years, they have been instrumental in the development of silicon devices that operate at 91% of their theoretical (Auger) limit. Lifetime testing, and the associated reconstruction of the implied-J-V curve, can moreover be performed at every cell-processing step, thus allowing a direct peek into the impact of that step on cell performance. Therefore, adapting these techniques and tools to non-Si devices would greatly improve their learning rate.

In this project, we developed a Suns-ERE technique—the equipment, methodology, and know-how—to measure the implied-J-V curve, the pseudo-J-V curve, and the actual J-V curve of a thin-film solar cell, allowing an accurate assessment of the quality of the bulk material and its surface passivation, the selectivity of the contact, and its resistivity. We used this technique to show that the absorber of present CdSeTe solar cells is capable of achieving 1 V Voc,, that passivation layers exist (e.g., Al2O3) that can support such high voltages, and that the barrier is identifying contact layers that are both passivating and carrier-selective.

The characterization platform created in this project and the understanding generated using it will accelerate the progress of non-silicon PV technologies. In particular, the project will contribute to CdSeTe solar cells with Voc > 1 V and cell efficiency > 24%. Such cells provide a pathway to module-level efficiencies >23%. As CdSeTe presently competes with silicon on module cost (in $/W) and yet has significantly more room for efficiency gains, the potential for LCOE reduction is particularly large. For example, CdTe modules with an efficiency of 21% would allow an LCOE below $0.04kWh^{-1} in average US climates.

Table of Contents:

Executive Summary **3**
Background **5**
Project Objectives **5**
Project Results and Discussion **8**
Significant Accomplishments and Conclusions **45**
Path Forward **45**
Products **46**
Project Team and Roles **47**
References **48**

Background:

Recent material improvements in polycrystalline cadmium telluride (CdTe) photovoltaic solar cells have increased both the effective minority-carrier lifetime τ and the acceptor (activated p-type dopant) concentration N_A. In particular, alloying CdTe with selenium (CdSeTe) has led to an increase in τ from a few nanoseconds to tens of nanoseconds.[1,2] Further, metal-oxide passivation layers—such as aluminum oxide (Al_2O_3) and magnesium zinc oxide (MZO)—can reduce recombination at the front and back interfaces, resulting in surface recombination velocities below 100 $cm.s^{-1}$ and lifetimes well above 100 ns.[3-6] Finally, arsenic doping has led to $N_A>10^{16}$ cm^{-3}—along with higher performance stability and lower degradation rates—thanks to reduced carrier compensation when compared with conventional copper-doped devices.[7-10]

Despite these materials innovations, the voltage—and, consequently, the efficiency—of polycrystalline CdSeTe devices remain low: the open-circuit voltage V_{oc} of record-efficiency devices is still below 900 mV and, thus, the bandgap-voltage offset $E_g/q–V_{oc}$ exceeds 500 mV. In comparison, record bandgap-voltage offsets are below 350 mV for competing thin-film technologies—such as perovskite and gallium arsenide (GaAs)—and below 400 mV for the best industrial crystalline silicon solar cells.[11-13] Thus, despite being the second-most manufactured solar cell technology, CdSeTe still has the largest headroom to improve. Device modeling indicates that these high bulk lifetimes, high acceptor concentrations, and low surface recombination velocities should, together, enable open-circuit voltages in excess of 1 V and efficiencies above 24%.[14-16] This mismatch between model predictions and experimental results raises the question of what limits the voltage of polycrystalline CdSeTe solar cells.

In particular, it remains unclear what the theoretical voltage limit $V_{oc,ideal}$ of CdSeTe absorbers is, and how Se alloying and As doping affect this limit; what the *internal* voltage iV_{oc} (or quasi-Fermi-level splitting: $QFLS = q \times iV_{oc}$, with q the elementary charge) of long-lifetime, high-acceptor-concentration CdSeTe devices with passivated surfaces is; and, finally, to what extent selectivity losses reduce the open-circuit voltage from iV_{oc} to $V_{oc.}$ In the crystalline silicon community, these questions are routinely answered to guide the development of high-efficiency devices using techniques such as quasi-steady-state photoconductance.[17,18] Similar techniques, often based on quantitative photoluminescence measurements, are now emerging for non-silicon thin-film devices, particularly perovskite solar cells.[19-22]

Project Objectives:

This project will develop, validate, and use a device characterization platform for non-silicon photovoltaic devices that will enable easy access to their implied open-circuit voltage (iV_{oc}) and fill factor (iFF), their pseudo fill factor (pFF) and thus series resistance (R_s) at maximum power point, and their complete-stack contact resistance (R_c). Together with calculated detailed-balance performance limits and traditional J-V measurements, these metrics will enable a precise accounting of recombination and resistive losses, from fundamental efficiency limits to experimental device performance, as shown in Fig. O1. The new or adapted characterization techniques that we will use to do this are given in

orange in Fig. O2; it is their synergistic use together that will enable the greatest advances over the present state of the art.

We will demonstrate the potential of this characterization platform by applying it first to CdSeTe solar cells with novel carrier-selective passivating hetero-contacts, starting from a contact stack consisting of an Al_2O_3 passivation layer in combination with a doped a-Si:H carrier-selective layer. The characterization platform will subsequently be applied to other absorbers, including perovskites. Using the developed analysis platform, this project will determine the actual iV_{oc} of very-high-lifetime passivated CdSeTe absorbers, and whether the proposed carrier-selective passivating contact stacks can finally push V_{oc} up to iV_{oc} in polycrystalline II-VI cells, thus revealing the unknowns highlighted in Fig. O1. Furthermore, we will refine this stack to reduce resistive losses – which will now be systematically measured – in order to maximize FF. Altogether, this systematic loss analysis will drive process and device architecture improvements in order to achieve CdSeTe devices with efficiencies in excess of 24%.

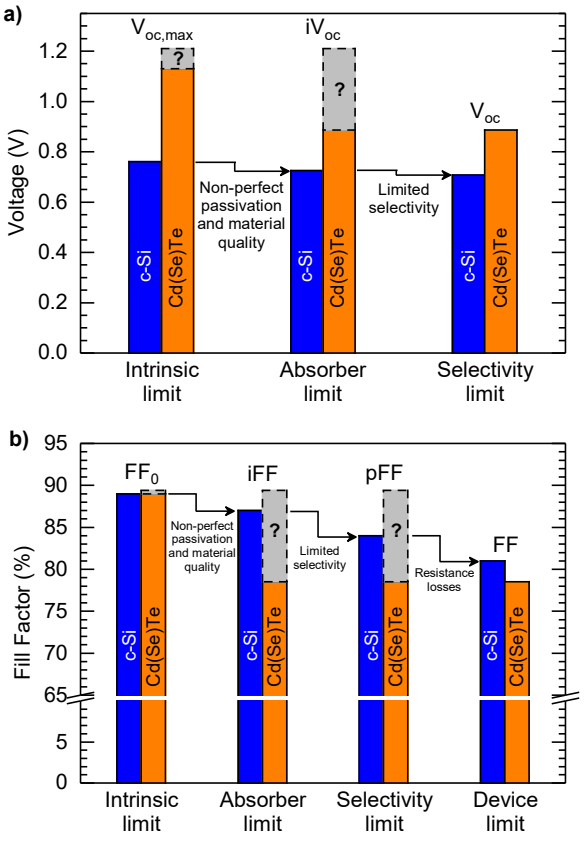

Fig. O1. Breakdown of losses from fundamental intrinsic limits to actual device performance, in terms of V_{oc} (a) and FF (b), for c-Si and Cd(Se)Te.

As described in greater detail below, this 3-year project is structured in two budget periods (BP), with BP1 corresponding to the two first years of the project and BP2 corresponding to the third (last) year:

- In BP1, the characterization platform will first be built and validated, using silicon heterojunction solar cells as a test system. In parallel, preliminary work will be undertaken in order to ensure a high enough CdSeTe material quality and surface passivation to achieve the final project goal (iV_{oc}>1 V). Once ready, the characterization platform will be used on CdSeTe absorbers, test contact structures, and devices to enhance key performance metrics (iV_{oc}, V_{oc}, R_s, and FF) through rapid iteration and systematic characterization.
- In BP2, the characterization platform will be extended to other absorber materials, including perovskites. Concurrently, full CdSeTe device integration will be undertaken, to demonstrate record-efficiency devices.

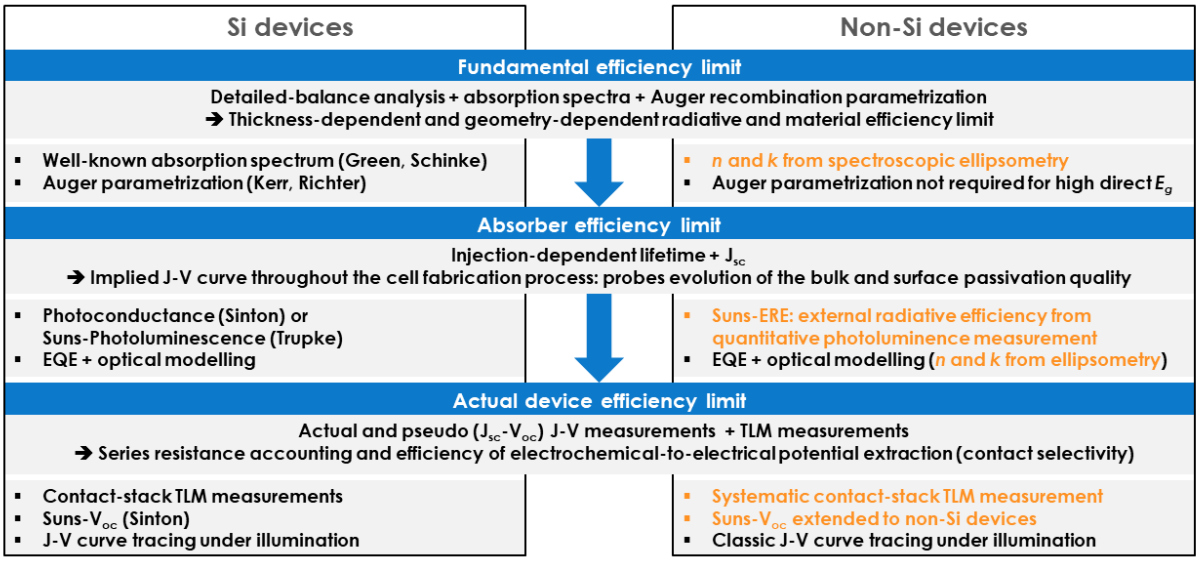

Fig. O2. Proposed characterization platform for full loss analysis of non-Si devices, from fundamental materials limits to actual efficiencies, by adapting metrics and techniques from the Si community (this project's contribution in orange).

To achieve its objectives, this project will pursue two intertwined, complementary tasks in parallel, throughout the three years of the project. Task 1 focuses on the building, validation, and demonstration of the characterization platform; the techniques to be developed or adapted are highlighted in orange in Fig. O2. Task 2 uses the characterization platform to rapidly optimize hole-selective contacts to high-material-quality CdSeTe absorbers and reach record efficiencies. The overall project organization is shown in Fig. O3; the Go/No-Go milestones, at the end of BP1, are indicated in red. These Go/No-Go milestones represent critical deliverables that are required for the overall project success and for the following BP2 steps and milestones. As a result, they strongly contribute to uncertainty reduction and risk mitigation in the project. Moreover, for both Tasks, we will pursue a step-by-step approach so that potential roadblocks can be eliminated one at a time.

The characterization platform (Task 1) will be tested and validated on simple material systems before extending it to increasingly complex ones:

1. Validation of new techniques on mature monocrystalline Si absorbers and silicon heterojunction (SHJ) solar cell devices
2. Validation of techniques that are sensitive to grain boundaries on small-grained multicrystalline Si absorbers and devices
3. Extension to homogeneous (non-graded) CdTe and CdSeTe absorbers and devices
4. Extension to vertically inhomogeneous (graded) CdSeTe absorbers and devices; the demonstration of the characterization technique on such complex absorbers and devices will be a Go/No-Go requirement to continue the project into BP2
5. Extension to complex materials, which may be spatially inhomogeneous in more than one dimension, such as perovskites and CIGS

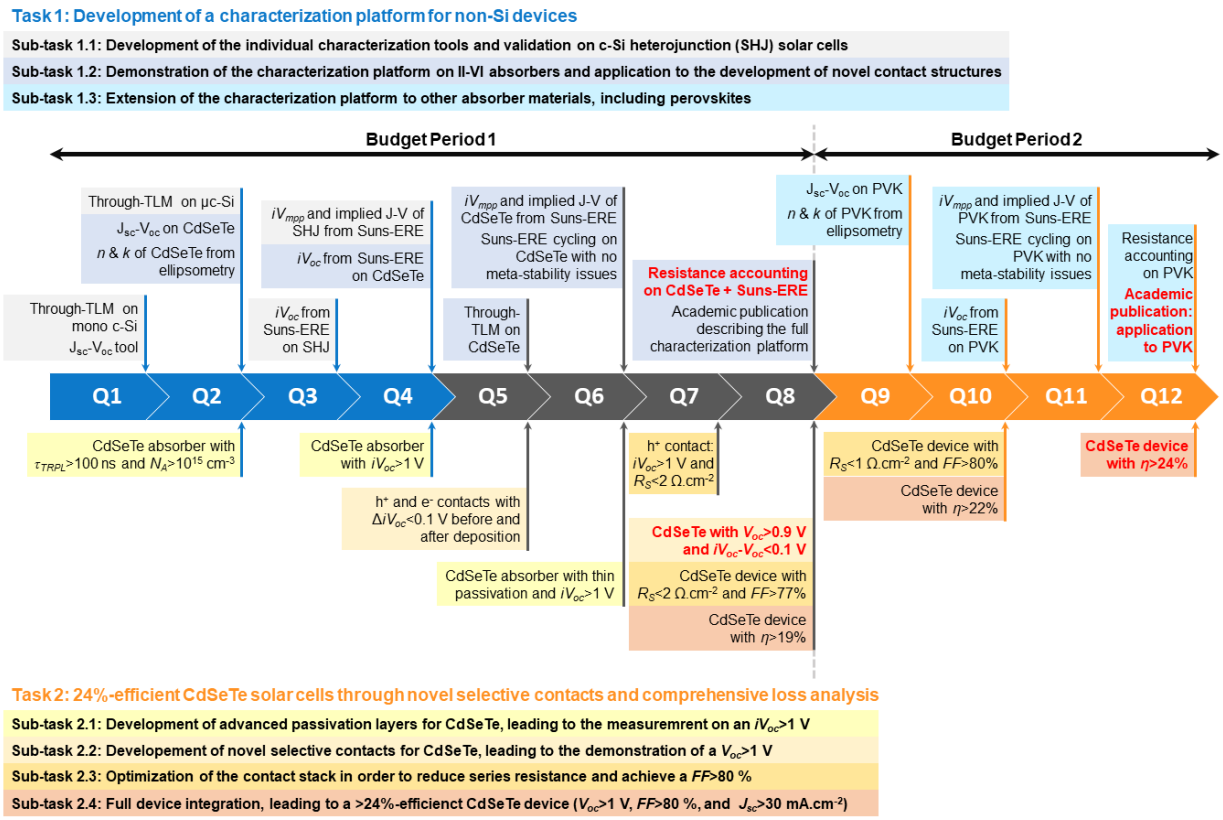

Fig. O3. Timeline of the Tasks, Subtasks, and milestones. The Go/No-Go milestones and end of project goals are in red.

Similarly, the development of novel hole-selective contacts to high-material-quality CdSeTe absorbers (Task 2) is organized so that potential bottlenecks are identified and eliminated early on:

1. The iV_{oc} will first be maximized by optimizing the absorber material quality and passivation
2. Carrier-selective contacts will then be developed and evaluated by comparing the iV_{oc} and the V_{oc}; the achievement of a V_{oc}>1 V will be a Go/No-Go requirement to continue the project into BP2
3. Optimization of the contact stack will be performed by identifying and minimizing sources of resistive losses.
4. Full device integration will finally be carried out.

Project Results and Discussion:

Task 1: Development of a characterization platform for non-Si devices

Sub-task 1.1: Development of the individual characterization tools (n and k, ERE, J_{sc}-V_{oc}, and TLM measurements) and validation on SHJ solar cells

Milestone 1.1.1: Validation of vertical TLM on SHJ cells (Q1)

In order to validate the vertical TLM method, we fabricated standard lateral TLM and vertical TLM structure side-by-side on mono-crystalline c-Si wafers, as shown in Figure

1. We deposited standard SHJ solar cell contacts (a-Si:H(i)/a-Si:H(n)/TCO/Ag), with different types of TCO: indium tin oxide (ITO), hydrogen-doped indium oxide (IO:H), and bi-layer IO:H/ITO.

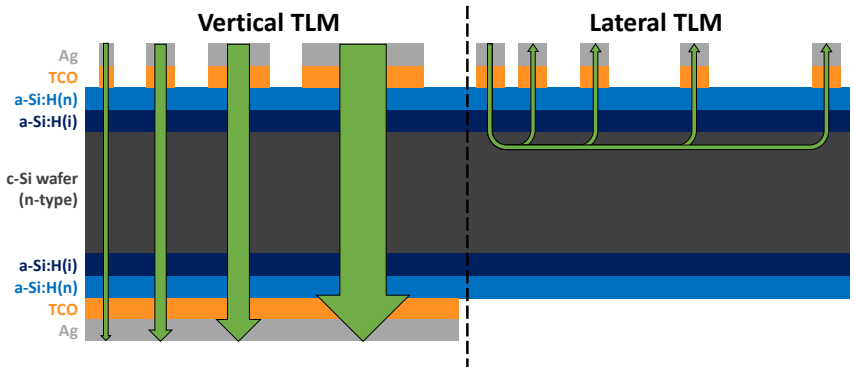

Figure 1. Structures used for comparison of vertical TLM and lateral TLM techniques. The green arrows indicate the current path through the test structures.

In the vertical TLM approach, assuming that the resistance through the wafer is inversely proportional to the area of the top contacting pad—i.e. resistance spreading is negligible as the width of the pads is larger by orders of magnitude than the thickness of the absorber—the specific total resistance of the full contact/absorber/contact stack can be determined precisely by a linear regression through the origin, as shown on Figure 2.

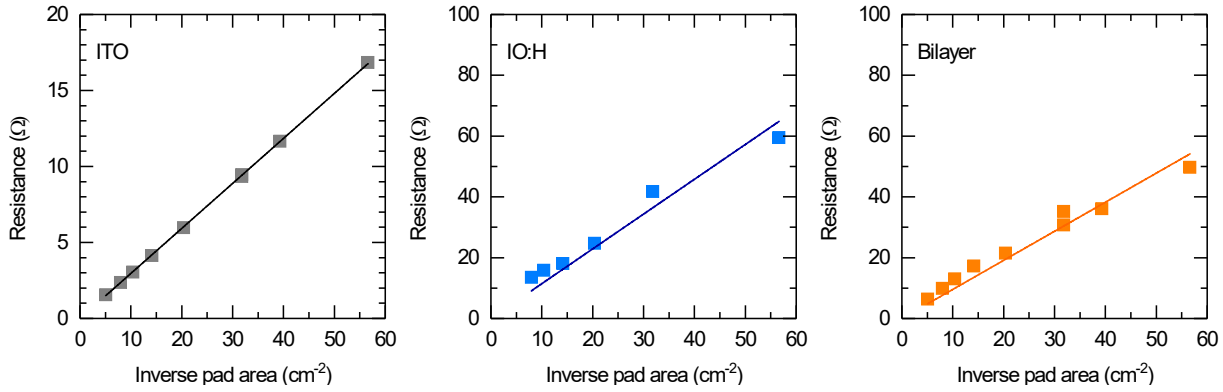

Figure 2. Resistance as a function of the inverse pad area for three different types of TCOs (ITO, IO:H, and ITO/IO:H bilayer) with linear fits through the origin.

In Figure 3, the specific total resistance of the stacks, measured by vertical TLM, are compared with the expected values calculated from the specific contact resistances and sheet resistances, extracted from standard lateral TLM measurements. The wide error bars are due to inhomogeneity issues encountered during deposition of the contact layers. However, the results from vertical TLM measurements fall within the error margin of the values calculated from lateral TLM measurements for all the structures tested, except for the ITO layers. The technique is thus initially validated, although care must be taken during processing to ensure homogeneity of the layers.

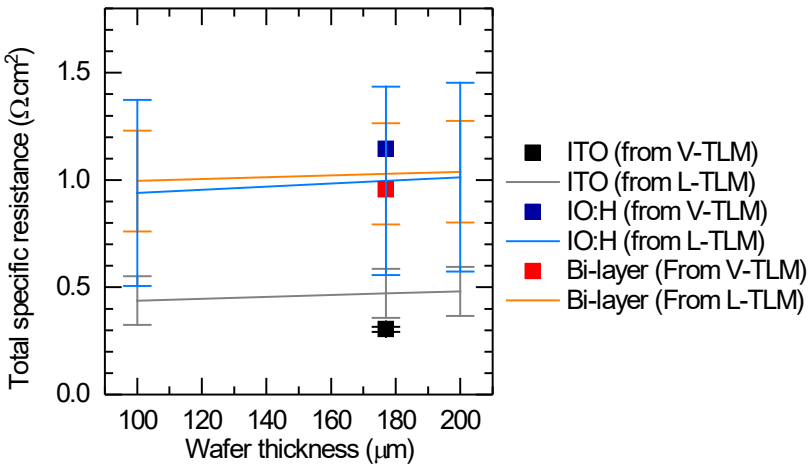

Figure 3. Total specific resistance of the full contact/absorber/contact stack as a function of the wafer thickness. The results obtained from vertical TLM measurements are shown as discreet values; the calculated values from lateral TLM measurements are shown as continuous lines.

Milestone 1.1.2: Validation of J_{sc}–V_{oc} technique on SHJ cells (Q1)

We performed J_{sc}–V_{oc} measurements on SHJ solar cells using a standard Newport Oriel (92193A-1000) AM1.5G solar simulator and neutral density filters obtained from Sinton Instruments. We recorded full *J*–*V* curves, using a Keithley 2440 source-meter, at each reduced illumination level. The J_{sc}–V_{oc} pairs recorded at each illumination level can then be converted into a pseudo-JV curves using the superposition principal:

$$J(V_{oc}) = J_{sc}^{1\,sun} - J_{sc}^{X\,sun}(V_{oc})$$

where $J_{sc}^{X\,sun}$ is the J_{sc} measured under a reduced illumination of X suns.

The results are shown in Figure 4, overlaying measurements performed using the J_{sc}–V_{oc} technique described above and measurements from a standard Sinton Suns-V_{oc} tool, where the equivalent J_{sc} is assessed using a separate monitoring c-Si cell instead of directly measured on the device to be characterized. The equivalence between the two techniques is demonstrated, with a maximal error of 5 mV between the two techniques, thus validating the technique and fulfilling the requirements of the milestone. The systematic error between the two techniques, shown in Figure 4, increases with increasing illumination intensity and is suspected to originate from the difference in sample temperature between constant illumination testing (J_{sc}–V_{oc}) and flash illumination testing (Suns-V_{oc}).

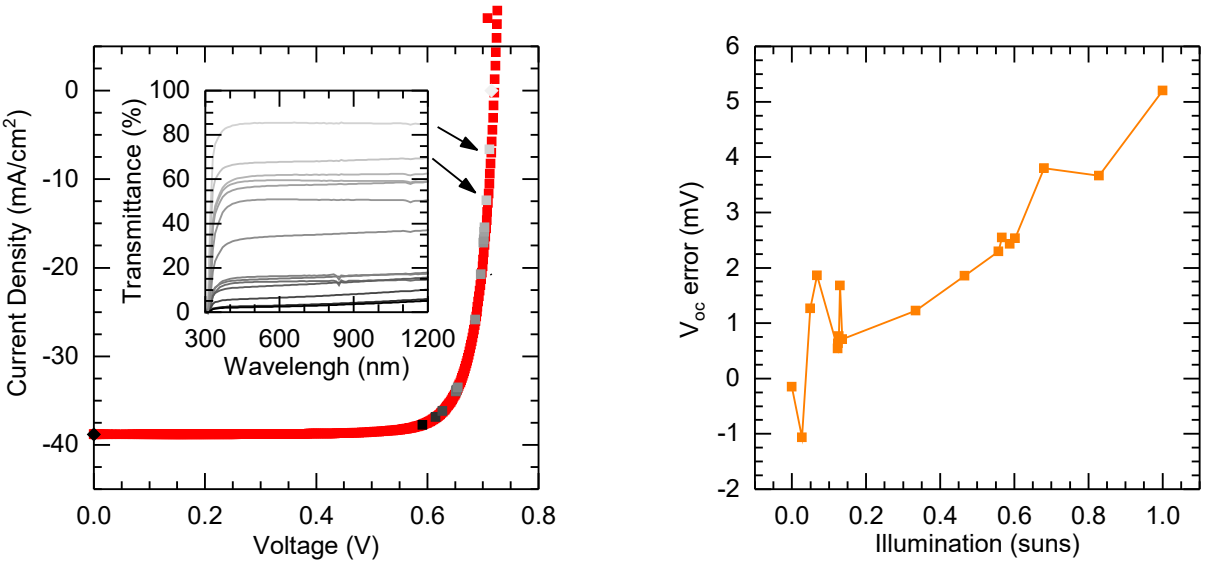

Figure 4. Left: Comparison between the results obtained using a Sinton Suns-V_{oc} tool (red dots) and the J_{sc}–V_{oc} technique (shades of gray). The transmission of the neutral density filters used for the J_{sc}–V_{oc} measurements are shown in the inset. Right: Error between the two measurements.

Milestone 1.1.3: Validation of vertical TLM on multi-crystalline SHJ cells (Q1)

In agreement with DOE, this milestone has been removed as it was providing limiting insights into the technique. Instead, it was decided to focus directly on Milestone 1.2.4 to demonstrate the technique on CdSeTe solar cells and contacts to such devices, starting with MZO.

Milestone 1.1.4: Measurement of iV_{oc} on an SHJ cell using the Suns-ERE technique (Q9)

Extracting the implied voltage of a sample from an external radiative efficiency (ERE) measurement requires two steps. First, the radiative voltage limit $V_{oc,ideal}$ under a given illumination level needs to be calculated according to:

$$V_{oc,ideal} = \frac{k_B T}{q} ln\left(\frac{J_{sc}^{X\ sun}}{J_{0,rad}}\right)$$

where $J_{0,rad}$ is the recombination current density associated with radiative recombination and $J_{sc}^{X\ sun}$ is the equivalent J_{sc} that would be measured under a reduced illumination of X suns—assuming the validity of the superposition principle. Detailed-balance analysis of the cell under thermal equilibrium (i.e. in the dark at room temperature) tells us that $J_{0,rad}$ is equal to the current density of photons emitted by the surrounding black body at room temperature and absorbed by the cell, so that:

$$J_{0,rad} = \int a(\lambda)\phi_{BB}(\lambda)d\lambda$$

where λ is the wavelength, $a(\lambda)$ is the wavelength-dependent absorptance of the absorber—equivalent to the EQE of the cell for cells with long enough diffusion length

and selective contact—and $\Phi_{BB}(\lambda)$ is the wavelength-dependent photon flux per surface area of the black body at room-temperature. Similarly, we have:

$$J_{sc}^{X\ sun} = \int a(\lambda)\phi_{X\ sun}(\lambda)d\lambda$$

with $\Phi_{X\ sun}(\lambda)$ the wavelength-dependent photon flux per surface area of a given illumination in suns-equivalent.

Both photon fluxes—from the sun and from the black body at room temperature—are well-know, tabulated for the former and easy to calculate for the latter. Thus, only the absorptance of the device is required to calculate its radiative voltage limit $V_{oc,ideal}$ in a given configuration (stand-alone film or wafer or fully fabricated cell). Such calculations require an excellent optical model of the device, taking into account front reflectance, escape reflectance, and parasitic absorption. Although such models can be hand-built using a set of reasonable assumptions, the process can be time consuming.

Instead, we use the commercial software SunSolve,[23] from PV Lighthouse, to rapidly and accurately simulate complex cell structures. Knowing the optical constants (*n* and *k*) and thickness of each individual layer of the device, a full model of even complex structures can easily be built. Ray-tracing techniques, built-in the software, are then used to determine the absorptance and, hence, the equivalent current density under different photon fluxes. The calculation of the J_{sc} under 1 sun is already included in SunSolve, without needing any additional input. For calculation of the $J_{0,rad}$, additional custom spectra for black bodies at 294.15 K (21 °C), 298.15 K (25 °C), and 300 K (26.85 °C) were calculated and uploaded on the SunSolve platform. That way, the $V_{oc,ideal}$ can be accurately determined in a matter of minutes.

In order to validate the technique, we simulated flat and textured GaAs absorbers of varying thickness and compared the calculated $V_{oc,ideal}$ with the results calculated by Miller *et al*.[24] Matching results were found (less than 5 mV difference), thus validating the use of SunSolve to calculate the $V_{oc,ideal}$ of absorbers.

Second, the ERE of the device (absorber or finished cell) needs to be determined. This is achieved using a quantitative photoluminescence (PL) measurement. The earlier system used for these measurements is detailed in Figure 5. To calibrate the system, a Lambertian reflector of known reflectance is placed on the sample stage. The measured signal I_{LR} is then given by:

$$I_{LR} = A \times \Phi_{laser} \times R_{LR}(\lambda_{laser}) \times S_{PD}(\lambda_{laser}) \times E_{laser}$$

with Φ_{laser} the photon flux beamed on the Lambertian reflector, $R_{LR}(\lambda_{laser})$ the reflectance of the Lambertian reflector at the laser wavelength λ_{laser}, $S_{PD}(\lambda_{laser})$ the photodetector response at the laser wavelength, $E_{laser}=hc/\lambda_{laser}$ the photon energy of the laser, and A a proportionality factor dependent on the PL system geometry.

Replacing the Lambertian reflector with the sample to be characterized—adding a long-pass filter between the sample and the photodetector to eliminate reflected photons—the signal measured I_{sample} is now:

$$I_{sample} = A \times \Phi_{reemitted} \times T_{LP}(\lambda_{sample}) \times S_{PD}(\lambda_{sample}) \times E_{g,sample}$$

with $\Phi_{reemitted}$ the flux of photons reemitted, $T_{LP}(\lambda_{sample})$ the transmittance of the long-pass filter at the emission wavelength of the sample λ_{sample}, $S_{PD}(\lambda_{sample})$ the photodetector response at the emission wavelength of the sample, $E_{g,sample}=hc/\lambda_{sample}$ the bandgap of the absorber, corresponding to the energy of reemitted photons, and A the same proportionality factor.

The ERE is then calculated the dividing the flux of photons beamed on the sample by the flux of photons reemitted, the proportionality factor cancelling out in the operation:

$$ERE = \frac{\Phi_{reemitted}}{\Phi_{laser}} = \frac{I_{sample} \times A \times R_{LR}(\lambda_{laser}) \times S_{PD}(\lambda_{laser}) \times E_{laser}}{I_{LR} \times A \times T_{LP}(\lambda_{sample}) \times S_{PD}(\lambda_{sample}) \times E_{g,sample}}$$

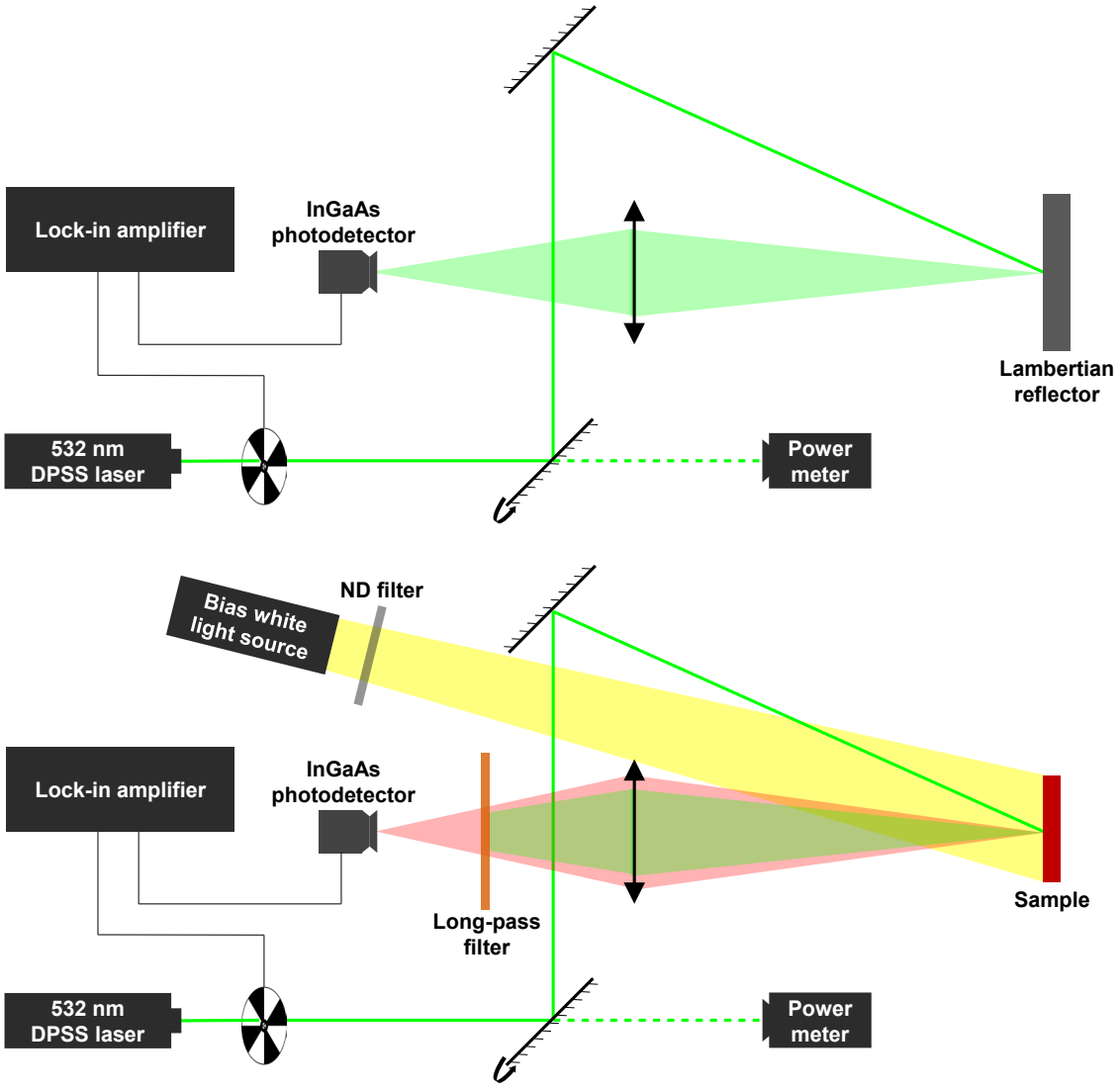

Figure 5. (Top) Earlier Suns-ERE system in calibration mode, with a Lambertian reflector of known reflectance on the sample stage. (Bottom) Earlier Suns-ERE system in measurement mode, with a white bias light source used to set the injection level to one sun.

In order to eliminate background noise and measurement errors due to parasitic photons, the laser beam is chopped with a classic mechanical chopper. A lock-in amplifier, connected to both the chopper controller and the photodetector, is then used to extract the chopped signal. As a result, measurements can be carried out under imperfect dark conditions (i.e. lights on). Moreover, an external bias light can then be used to set the injection level.

Indeed, the injection level and, thus, the equivalent number of suns, can be set by two different approaches: 1) by adjusting the power of the laser and 2) by using a low laser power and a bias light. The only requirement for this second approach is that the photon flux of the laser needs to be orders of magnitude (at least a hundred times) smaller than the photon flux from the bias light.

The advantages of using a bias light are multiple:

- A white bias light, leading to a generation profile close to AM1.5G test conditions, can be used, thus allowing a measurement as close as possible to realistic test conditions
- The calibration of the system with the lambertian reflector only needs to be carried out once, instead of recalibrating the system at each laser power
- For samples with long minority-carrier diffusion length, such as good silicon solar cells, the injection level is uniform across the sample and the comparatively small laser spot does not lead to an uneven increase in carrier concentration in the area surrounding the laser spot (spreading of carriers outside the excitation spot).

The implied (internal) open-circuit voltage iV_{oc} is then given by:

$$iV_{oc} = V_{oc,ideal} + \frac{k_B T}{q} ln(ERE)$$

To validate the use of the Suns-ERE technique at one-sun-equivalent to determine iV_{oc}, we have compared the results obtained on two unfinished SHJ cells using Sinton WCT-120 QSSPC tool and Suns-ERE. The results are detailed in Table 1. Unfinished cells, with intrinsic and doped a-Si:H layers but no electrode (i.e. no ITO and no metal) were used, as iV_{oc} cannot be measure by QSSPC on metallized samples (the conductance of the metal layer dominates the measurement).

Sample	**SHJ cell 1**	**SHJ cell 2**
$V_{oc,ideal}$ (mV)	857.9	857.9
ERE (%)	0.86	0.81
iV_{oc} from ERE (mV)	737.3	735.8
iV_{oc} from QSSPC (mV)	736.2	731.3
Absolute difference (mV)	1.1	4.5
Relative difference (%)	0.15	0.62

Table 1. Comparison of iV_{oc} calculated by ERE and QSSPC, demonstrating an agreement within ±5 mV between the techniques.

As shown in Table 1, the agreement between the two techniques is within ±5 mV, thus validating the use of the Suns-ERE technique at one-sun-equivalent to determine iV_{oc}.

Milestone 1.1.5: Reconstruction of the implied J-V curve of a SHJ cell, from 0.02 suns to 2 suns (Q4)

Using the superposition principle,[25] the Suns-ERE technique can be used at various suns-equivalent to determine the implied voltage as a function of the injection and, thus, reconstruct the implied J–V curve. In practice, this is achieved by calculating $V_{oc,ideal}^{X\ suns}$ under illumination from:

$$V_{oc,ideal}^{X\ suns} = V_{oc,ideal}^{1\ sun} + \left(\frac{k_B T}{q}\right)\ln(X)$$

and by measuring the ERE at different illumination levels, using neutral-density filters or an variable-intensity with bias light source to achieve the desired light intensity. Equation (2), detailed above, is then used to determine the implied voltage under varying illumination. The reconstructed implied J–V curve from Suns-ERE measurements can then be compared with the one obtained from Sinton WCT-120 QSSPC tool, as shown in Figure 6.

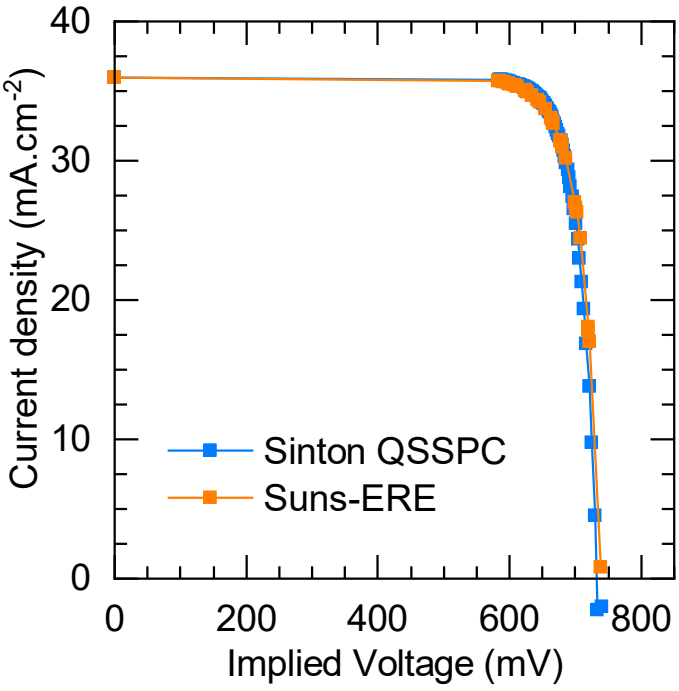

Figure 6. Comparison between the implied J–V curves reconstructed from QSSPC and Suns-ERE measurements.

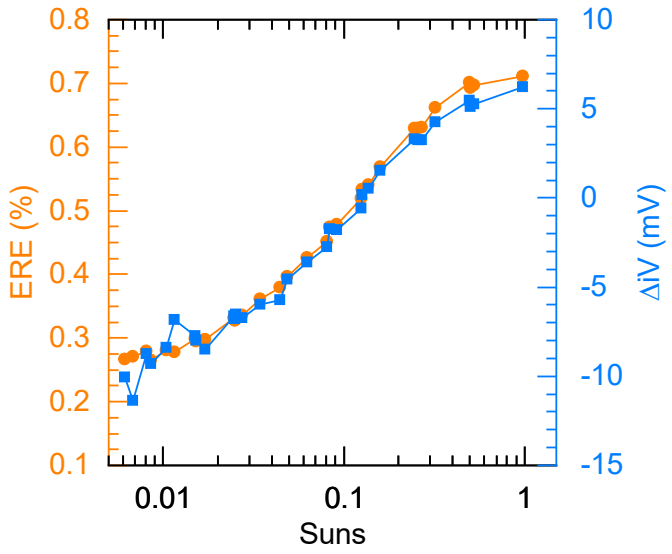

Figure 7. Comparison between the implied J–V curves reconstructed from QSSPC and Suns-ERE measurements.

The ERE as a function of the illumination, as well as the difference between the two measurements (in mV), are displayed in Figure 7. Throughout the range of illuminations tested (0.006 to 1 sun) the difference is below 10 mV, thus validating the Suns-ERE technique for the range of illuminations in question. A systematic error is present in the measurement, with the difference between the two techniques increasing with increasing illumination.

In order to understand the origin of this difference, we investigated the role of variations in carrier lifetime across the wafer with both measurements. Results from a first sample are shown in Figure 8, with the Suns–ERE measurement taken at a random position on the wafer and five QSSPC measurements taken across the wafer (four corners and center) with the WCT-120 tool.

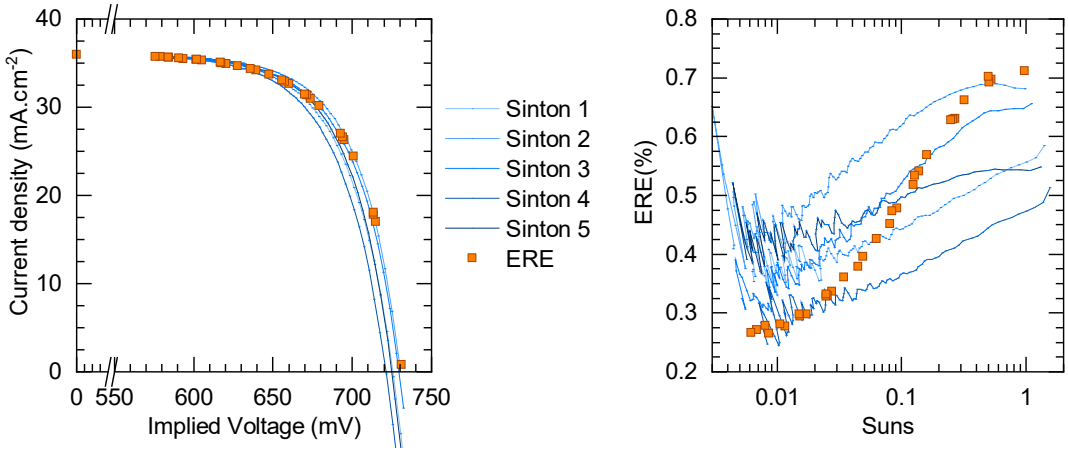

Figure 8. (Left) Comparison between implied J–V curves obtained with the Suns–ERE method and the Sinton QSSPC tool, with one measurement taken for the former and five measurements taken in five different positions across the wafer sample for the latter. (Right) Equivalent Suns–ERE curves.

Although the difference between the implied voltages obtained from ERE and QSSPC is below 10 mV—within the range required to achieve Milestone 1.1.5—the shape of the implied *J–V* curves is different. This effect is more visible on the equivalent Suns–ERE curves. As a result, although the same implied open-circuit voltage (iV_{oc}) is obtained from both techniques (within 10 mV) the implied fill factor (*iFF*) differs non-negligibly: 83.8–84.5% from QSSPC; 83.1% from Suns–ERE. However, as seen in Figure 8 (Left), variations across the wafer, as well as input parameters into both models ($V_{oc,ideal}$ for Suns–ERE; wafer thickness and doping density for QSSPC), can lead to sizable differences in results.

In order to control these parameters, we reproduced this validation experiment using a smaller 4 cm by 4 cm sample with homogeneous luminescence (±15% across the sample). We determined the exact thickness and resistivity of the sample beforehand through weight and 4-probe measurements. The results of this second validation experiment are shown in Figure 9. The agreement between the implied *J–V* curves and Suns–ERE curves is improved, with a mismatch in *iFF* reduced to 0.3% (81.9% from Suns–ERE, 82.2% from QSSPC) and a close match in iV_{oc} (725.5 mV from Suns–ERE, 723.0 mV from QSSPC).

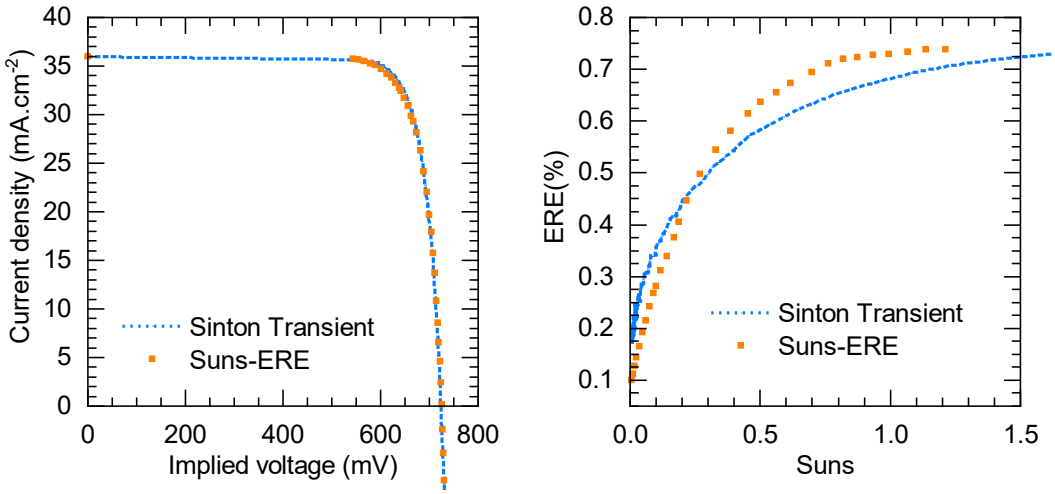

Figure 9. (Left) Comparison between implied J–V curves obtained with the Suns–ERE method and the Sinton QSSPC tool, with careful control of measurement parameters. (Right) Equivalent Suns–ERE curves.

Sub-task 1.2: Demonstration of the characterization platform on Cd(Se)Te absorbers and application to the development of novel contact structures

Milestone 1.2.1: Demonstration of the J_{sc}–V_{oc} technique on Cd(Se)Te cells (Q6)

Early J_{sc}–V_{oc} tests were conducted on Cd(Se)Te cells. The results are shown in Figure 10, showing that the technique is readily transferrable without particular issues.

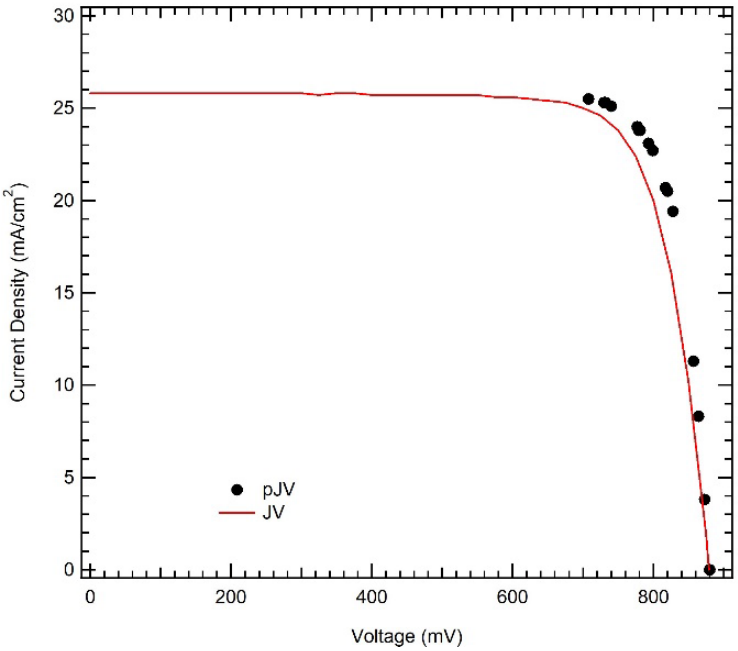

Figure 10. Pseudo and actual J-V curves on a Cd(Se)Te device. The pseudo J-V curve was reconstructed from J_{sc}–V_{oc} measurements.

In order to show the repeatability of the technique and that the measurement does not trigger any meta-stability in the device, the measurement was repeated on multiple days on two Cd(Se)Te cells with distinct structures (a baseline CdSeTe device and a thin CdTe device). The results for the first five days of measurements are shown in Figure 11.

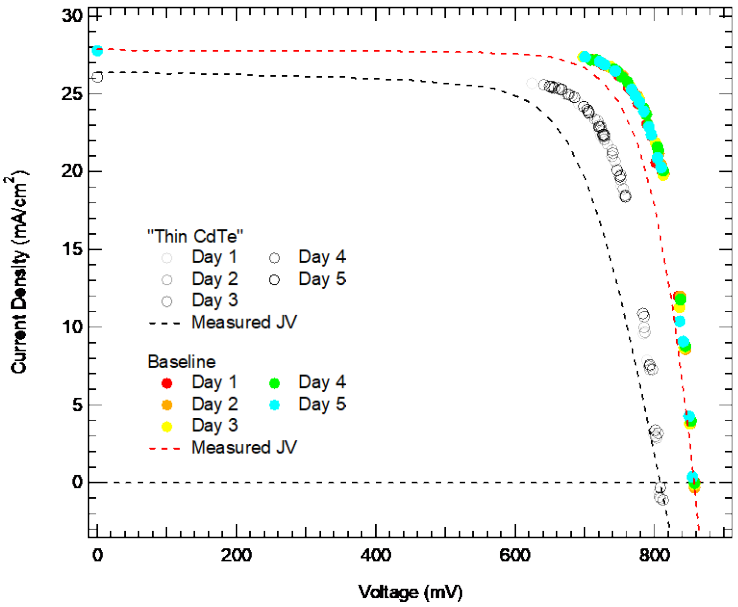

Figure 11. Pseudo J–V curves, reconstructed from J_{sc}–V_{oc} measurements carried out over five consecutive days, along with actual (i.e. classic) J–V for a baseline CdSeTe cell and a thin CdTe cell.

For both cells, the measurement proves to be reproducible and does not appear to trigger any meta-stability, thus validating Milestone 1.2.1. As shown in Figure 12, changes in the results of these measurements only occurred after five days, upon the inset of degradation of the device. Particularly, this degradation process is associated with a decrease in shunt resistance, which affects both the actual and pseudo J–V curves and is clearly visible on Figure 12. Thus, the loss of repeatability is not only due to a phenomenon external to the measurement, but also informs us on the nature and the origin of the degradation.

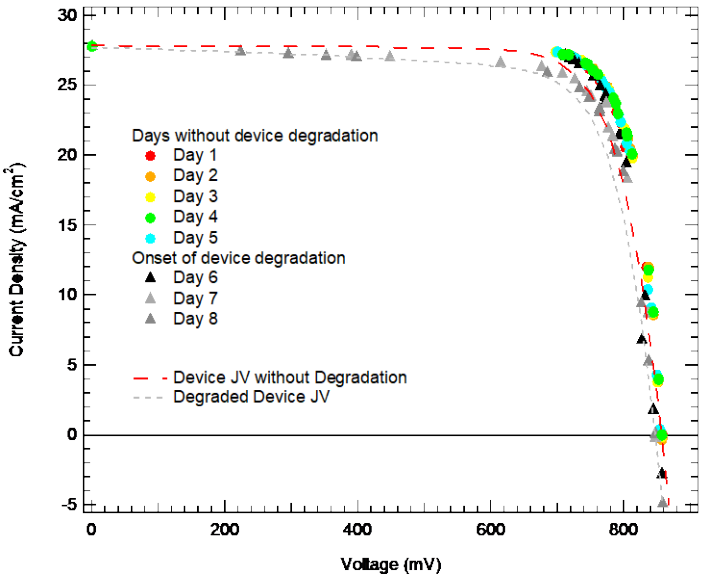

Figure 12. Pseudo and actual J–V curves for the baseline CdSeTe device from measurements carried over eight days. Degradation onsets after the fifth day.

Milestone 1.2.2: Determination of the *n* & *k* and optical modeling of Cd(Se)Te absorbers and devices (Q2)

To determine the optical parameters of CdTe and CdSeTe (with a 40%/60% Se/Te ratio), we use a combination of spectrophotometry and spectroscopic ellipsometry. As described by Manzoor *et al.*,[26] the Ψ and Δ data from ellipsometry and the absorptance and reflectance data from spectrophotometry are first simultaneously fitted using B-spline functions. These mathematical artifacts allow accurate description of the features of the dielectric function of the films while conserving Kramers-Koenig consistency (*i.e.*, the description of the films with B-spline is physical). Oscillators can then be fitted onto these B-splines.

This approach requires development of an accurate optical model of each individual layer of the full contact stack: a model is first developed for the bare TEC-10 substrate, then for MZO (electron contact) on TEC-10 and for CdTe or $CdSe_{0.4}Te_{0.6}$ on bare TEC-10, then a model of the full sample stack (TEC-10/MZO/Cd(Se)Te) is constructed. An effective medium approximation (EMA) layer is used at the top on the sample stack to model the impact of the surface roughness of the CdTe and CdSeTe films. The difference in bandgap between CdTe and $CdSe_{0.4}Te_{0.6}$ is visible in Figure 13, with the extinction

coefficient *k* going to zero at lower energies in the presence of Se and a correlated shift in the first oscillator peak around 1.5 eV.

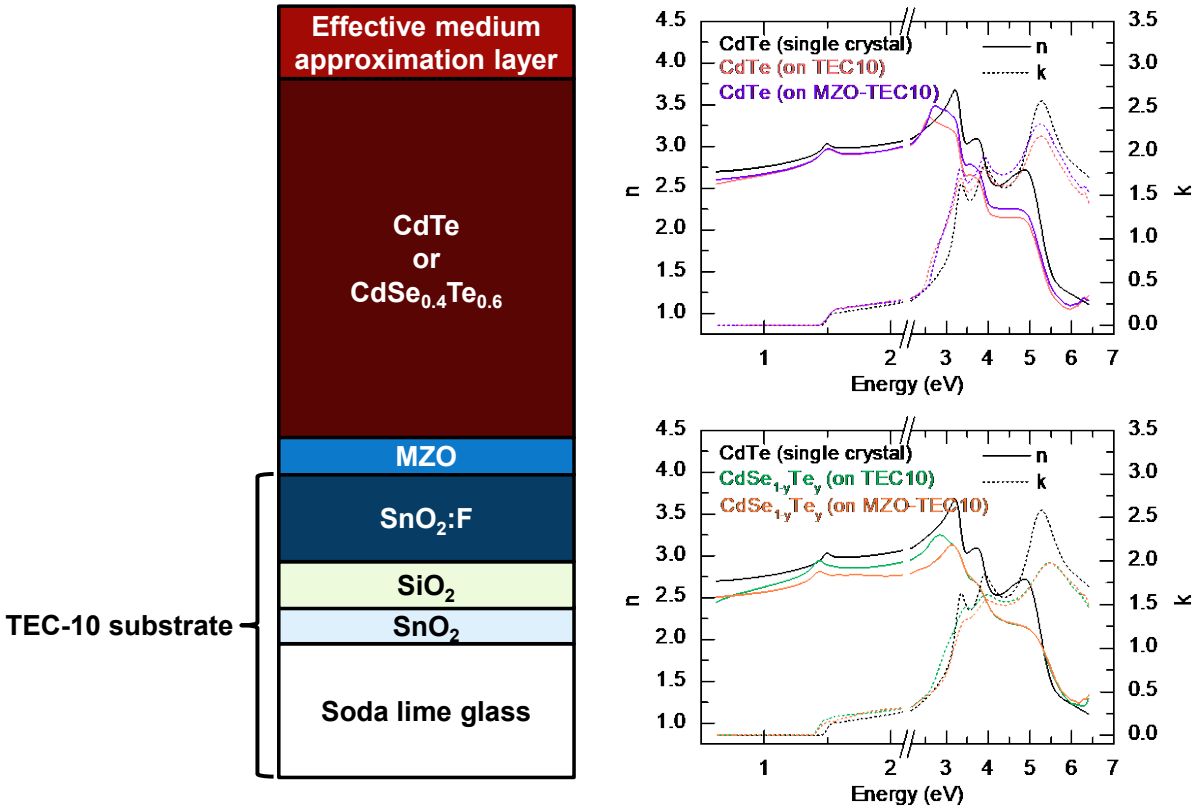

Figure 13. a) Structure of the samples measured and modeled, the effective medium approximation layer at the top of the stack is used to model the impact of the film surface roughness. b) Optical parameters extracted for CdTe on TEC-10 and TEC-10/MZO, compared with single-crystal CdTe data from the literature. c) Optical parameters extracted for $CdSe_{0.4}Te_{0.6}$ on TEC-10 and TEC-10/MZO, compared with single-crystal CdTe data from the literature.

Using these parameters, we reproduced the absorptance of a complete CdSeTe/CdTe device with a Al_2O_3/a-Si:H(p)/ITO/Ag back contact using the commercial software SunSolve.[27] The device structure and simulation results are displayed in Figure 14, comparing the modeled absorptance with the measured EQE, with the underlying assumption of unity collection efficiency (*i.e.*, all charge carriers photogenerated in the absorber are collected at short-circuit and the EQE matches the absorptance). The good agreement between the two EQEs, with a difference between the measured and modeled J_{sc} below 3% (28.0 mA.cm^{-2} measured, 27.3 mA.cm^{-2} modeled), validates our *n* and *k* parameters for CdTe and CdSeTe. As shown on the modeled device structure, we used effective thicknesses for the CdSeTe and CdTe layers as SunSolve cannot model graded absorbers.

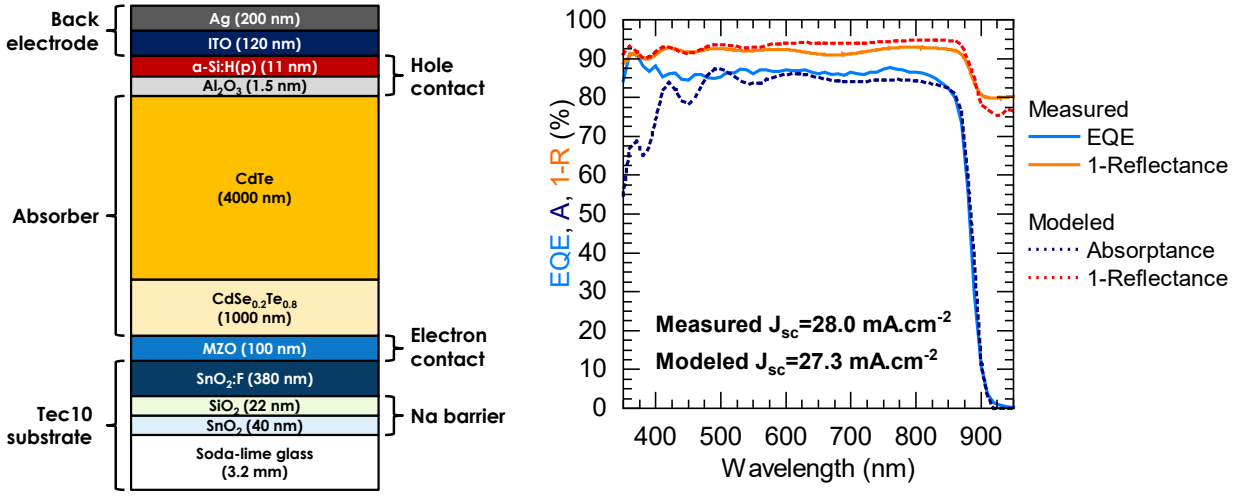

Figure 14. (Left) Structure of the device modeled. (Right) Comparison between The modeled and measured EQE and 1–R.

Milestone 1.2.3: Determination of the iV_{oc} on CdSeTe absorbers and devices using ERE at one sun (Q4)

As for c-Si, determining iV_{oc} in CdSeTe absorbers and devices requires measurement of the ERE and calculation of $V_{oc,ideal}$. However, CdSeTe devices usually include a graded absorber, which is hard to model accurately. Furthermore, as is shown below, the band edge of these finished devices can vary depending on the doping treatment performed, leading to strong changes in the band edge absorption of the device and, consequently, in $V_{oc,ideal}$.

Consequently, we used the EQE spectrum of finished devices to calculate their $V_{oc,ideal}$ and, hence, access their iV_{oc}. As described above, the underlying assumption is that $a(\lambda) = EQE(\lambda)$, meaning that the diffusion lengths of electrons and holes are longer than the thickness of the absorber and current extraction barriers are negligible. $V_{oc,ideal}$ is then calculated from:

$$V_{oc,ideal} = \frac{k_B T}{q} \ln\left(\frac{\int EQE(\lambda)\Phi_{AM1.5G}(\lambda)d\lambda}{\int EQE(\lambda)\Phi_{BB}(\lambda)d\lambda}\right)$$

As the AM1.5G photon flux varies slowly in the wavelength range of the band edge of CdSeTe, modification of the onset and shape of the band edge has a minimal impact (a couple mA.cm^{-1} maximum) on the short-circuit current density J_{sc} of the device—the numerator in the logarithm in the equation giving $V_{oc,ideal}$. On the other hand, as shown in Figure 15a, the black-body photon flux at room temperature increases quasi-exponentially with wavelength in the surroundings of the band edge, as it follows Planck's relation:

$$\Phi_{BB}(\lambda) = \frac{2\pi c}{\lambda^4} \frac{1}{exp\left(\frac{hc}{\lambda k_B T}\right) - 1}.$$

Consequently, any change in the onset and the shape of the band edge has a strong impact (potentially several times) on the radiative dark recombination current $J_{0,rad}$—the

denominator in the logarithm in the equation giving $V_{oc,ideal}$. As a result, the effective bandgap of the absorber is shifted and the radiative voltage limit $V_{oc,ideal}$ varies accordingly.

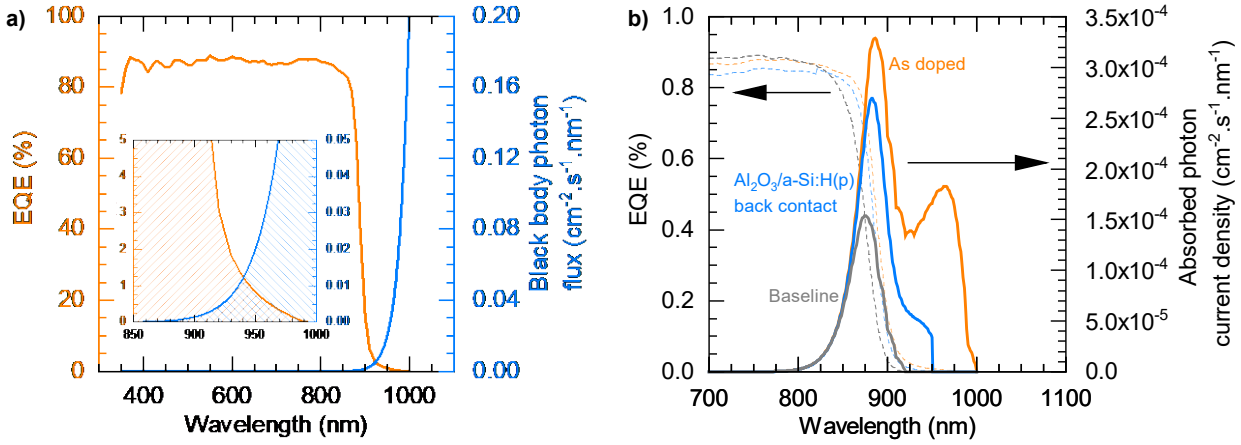

Figure 15. a) EQE of an As-doped CdSeTe device and black-body photon flux as a function of wavelength. The inset shows a zoom on the band tail, where the black-body photon flux increases by orders of magnitude. b) EQE and product $EQE \times \Phi_{BB}$ as a function of the wavelength for different CdSeTe devices, showing the impact of the band edge and band tails on the radiative dark recombination current $J_{0,rad}$.

This can be visualized in Figure 15b, comparing the product $EQE \times \Phi_{BB}$ for different devices; the area under the curve for each device corresponds to the radiative dark recombination current $J_{0,rad}$ and has a considerable impact on $V_{oc,ideal}$. In the cases presented in Figure 15b, the band edge shifts when changing the back contact from a standard Te/C-Ni structure to an Al_2O_3/a-Si:H(p)/ITO/Ag contact stack, leading to a 74% increase in $J_{0,rad}$ and an associated 11 mV decrease in $V_{oc,ideal}$. Even worse, when doping a sample with As, the band edge shifts further and detrimental band tails appear, leading to a 280% increase in $J_{0,rad}$ and an associated 30 mV decrease in $V_{oc,ideal}$.

Sample	$J_{0,rad}$ (mA.cm^{-2})	$V_{oc,ideal}$ (mV)	ERE (%)	iV_{oc} (mV)	ERE to reach iV_{oc}=1 V (%)
As-doped	4.26×10^{-18}	1115	0.27	963	1.2
Al_2O_3/a-Si:H(p) back contact	1.95×10^{-18}	1134	0.22	977	0.55
Baseline	1.12×10^{-18}	1145	0.02	929	0.33

Table 2. $J_{0,rad}$, $V_{oc,ideal}$, ERE, and iV_{oc} of the devices shown in Figure 15b, along with the ERE required from each device to reach iV_{oc}=1 V.

The $J_{0,rad}$, $V_{oc,ideal}$, *ERE*, and iV_{oc} for each device are shown in Table 2. Although the As-doped sample presents a higher ERE, it is not enough to offset the decrease in $V_{oc,ideal}$ due to the shift in band edge and the onset of band tails; the Cu-doped sample with an Al_2O_3/a-Si:H(p)/ITO/Ag back contact ends up having a higher iV_{oc}. High lifetime and majority carrier concentration—which should both boost iV_{oc}—have been reported with

As-doping of CdSeTe absorbers.[8] Yet the impact of the associated shift in band edge and onset of band tails—which, conversely, decrease the effective bandgap and, hence, the iV_{oc}—was not yet quantified. In the end, achieving iV_{oc}>1 V not only requires increasing the luminescence of the samples (i.e. the *ERE*) by orders of magnitude but also to keep the band edge and band tails of the absorber under control.

As shown in Figure 16, the band tails due to As doping are also responsible for the onset of a second photoluminescence peak. Indeed, the photoluminescence spectrum is directly related to (and can be predicted by) the product $a \times \Phi_{BB} = EQE \times \Phi_{BB}$.[28,29]

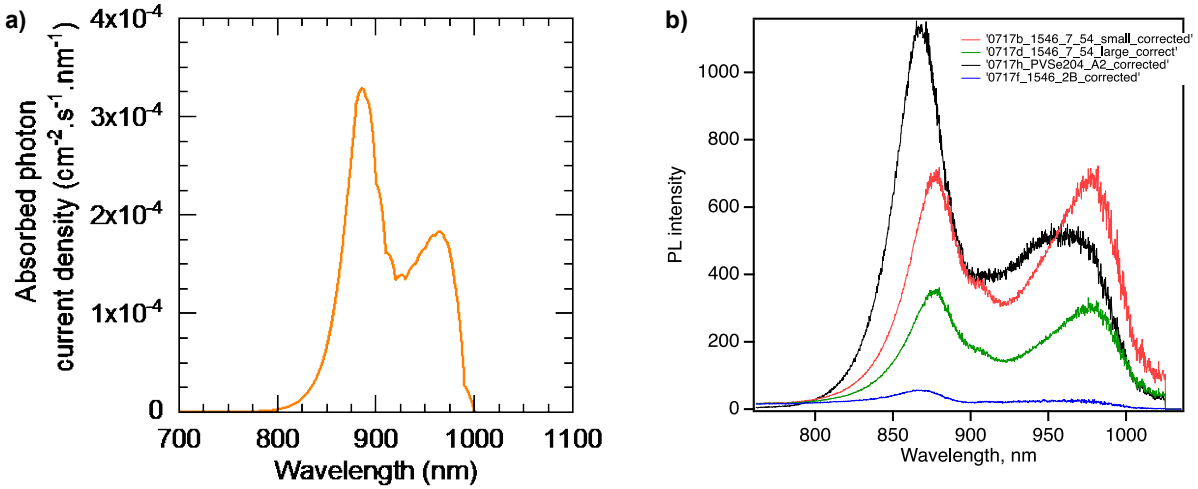

Figure 16. a) $EQE \times \Phi_{BB}$ product as a function of wavelength for the As-doped device, with a second peak due to bandtails. b) Photoluminescence spectrum for the same device (black).

Milestone 1.2.4: Determination of the specific contact resistance of contacts to CdSeTe absorbers using the vertical TLM technique (Q5)

In order to demonstrate the vertical transfer length measurement (V-TLM) method on thin-film samples, our work first focused on using it to determine the specific contact resistance of the interface between indium tin oxide (ITO) and magnesium zinc oxide (MZO) and the resistivity of MZO. To that end, samples with MZO layers of variable thickness sandwiched between a Ni/ITO bottom electrode and a ITO/Ag top electrode were fabricated. In these samples, the bottom electrode covers the whole glass substrate area, whereas circular pads of variable radius were used for the top electrode, as shown in Figure 17 (Left). A picture of a sample being measured is also shown on Figure 17 (Right).

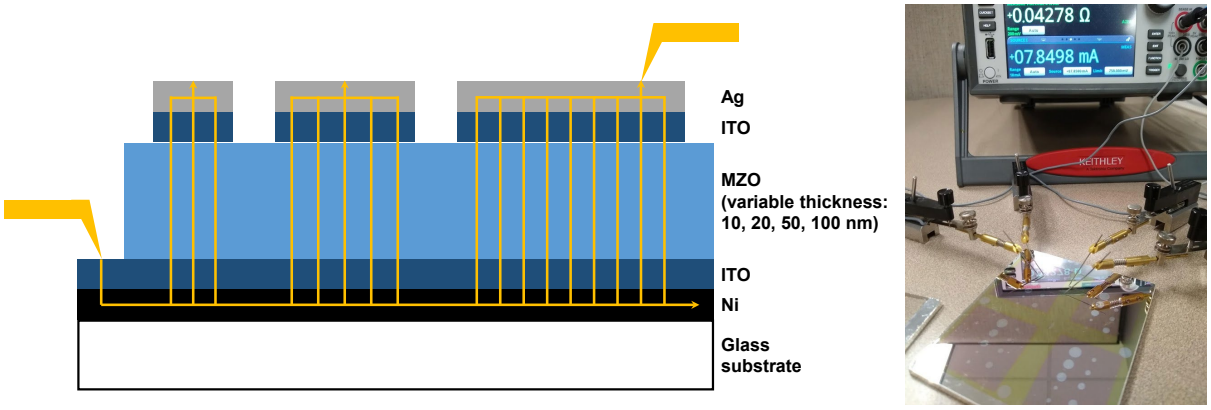

Figure 17. Sample structure used for the V-TLM measurements. The path of current is shown in yellow

In such structures, the lateral conductivity through the bottom electrode is the main source of uncertainty. Indeed, resistance through the bottom electrode sheet layer leads to a substantial residual resistance. Consequently, as shown in Figure 18, the total resistance does not tend toward zero when the inverse pad area tends towards zero (*i.e.*, the resistance with an infinite pad area is not equal to zero). Furthermore, if the distance between the bottom probe and the top probe varies—meaning that the lateral resistance through the bottom electrode is not constant—this residual resistance increases the uncertainty of the measurement with increasing pad area

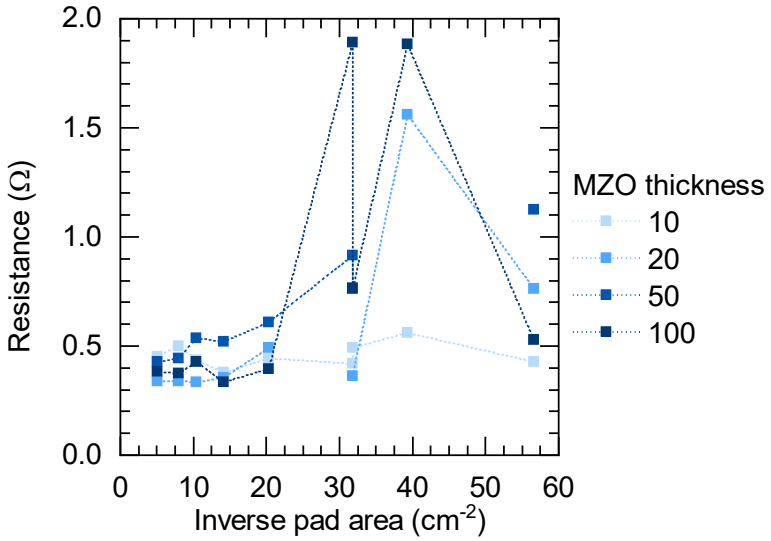

Figure 18. Resistance as a function of the inverse top electrode pad area for varying MZO thicknesses.

However, by fitting the curve for each MZO thickness, the impact of this residual resistance can be reduced to some extent. The slope of the fit—corresponding to the total specific resistivity of the structure ρ_{total}—is, in theory, directly related to the specific contact resistance of the MZO/ITO interface $\rho_{c,MZO/ITO}$, the MZO thickness t_{MZO}, and the resistivity of MZO ρ_{MZO} through a classic TLM linear relationship:

$$\rho_{total} = \rho_{MZO} t_{MZO} + 2\rho_{c,MZO/ITO}$$

The result for our set of samples is displayed in Figure 19, showing the slope fit from each curve in Figure 18 (*i.e.*, the specific total resistivity ρ_{total}, in $\Omega.cm^2$) as a function of the MZO thickness. Although uncertainty due to the residual resistance remains, leading to a non-linear relationship between t_{MZO} and ρ_{total}, upper and lower bounds for both $\rho_{c,MZO/ITO}$ and ρ_{MZO} can be determined: $\rho_{c,MZO/ITO} < 7$ $m\Omega.cm^2$; 300 $\Omega.cm < \rho_{MZO} < 3000$ $\Omega.cm$.

The low total specific resistivity of this test structure—below 20 $m\Omega.cm^2$ including the contribution of a relatively thick MZO layer—ensures that we can move to the next step: include CdSeTe to the test structure to probe the specific resistivity of the CdSeTe/MZO interface and the bulk resistivity of CdSeTe. In these future experiments, the contribution of the residual resistance will be controlled by increasing the conductivity of the bottom sheet electrode—by increasing its thickness—and by ensuring the same distance between the top and bottom electrode pads.

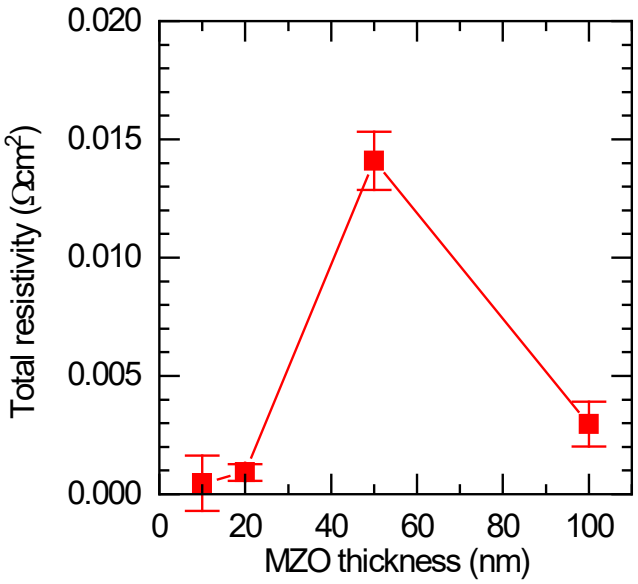

Figure 19. Specific total resistivity of the Ni/ITO/MZO/ITO/Ag structure as a function of the MZO thickness

Milestone 1.2.5: Reconstruction of the implied J–V curve of CdSeTe devices (Q6)

In order to rapidly measure the *ERE* of CdSeTe devices under variable illumination and, thus, reconstruct the implied *J–V* curve of such samples, a new version of the Suns–ERE tool has been built, with the goals of increasing its detection limit and simplifying its operation. A schematic of the revised tool design is shown in Figure 20.

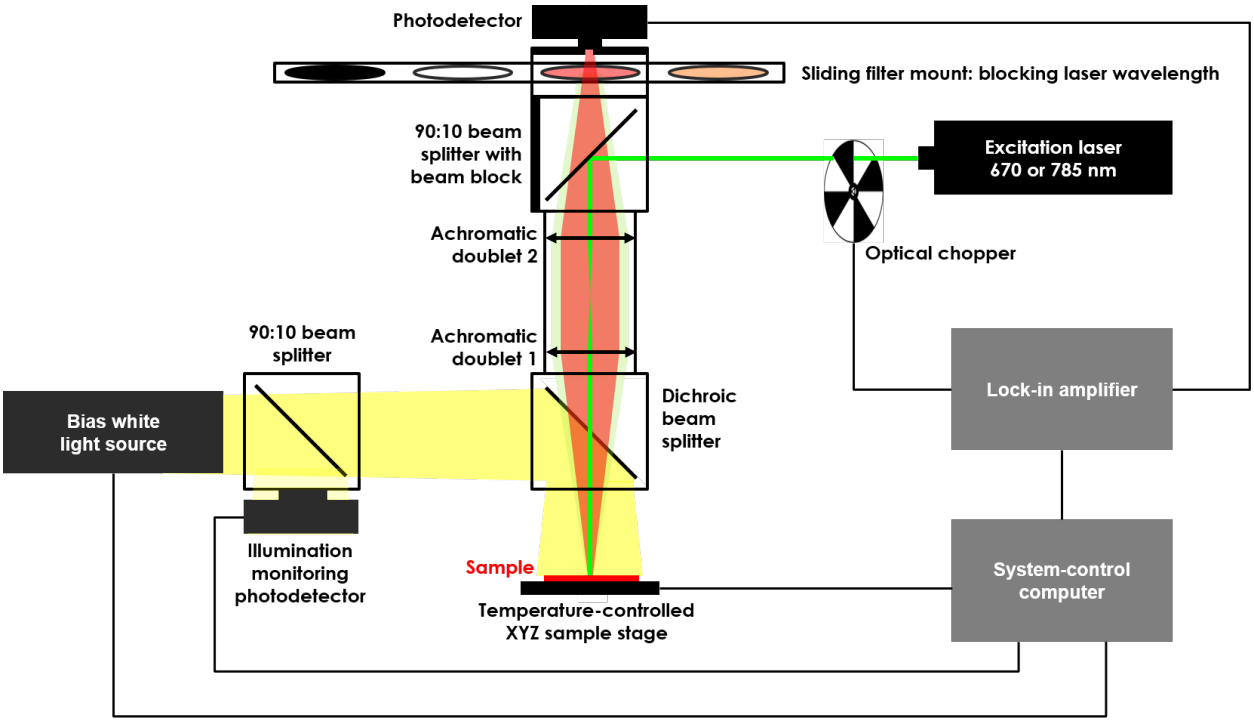

Figure 20. Schematic of the new Suns–ERE tool.

Central to this design is the use of a dichroic filter to decouple the optical paths of the white bias light on one side and of the excitation laser and photodetector on the other side. Consequently, the distance between the sample and the photodetector can be reduced and the field of view of the photodetector onto the sample is increased, thus improving the collected signal and, consequently, the sensitivity of the tool.

The tool includes 2 excitation lasers at wavelengths of 670 nm and 785 nm with a corresponding set of long-pass filters and dichroic beam splitters. The shorter-wavelength laser (670 nm) is used to probe high-bandgap samples, such as 1.7-eV perovskite absorbers and cells used in perovskite/silicon tandem devices. The longer-wavelength laser (785 nm) is used for lower-bandgap materials such as CdSeTe and c-Si. The current detection limit of the tool is ERE=0.001%, corresponding to non-radiative losses of approximatively 300 mV and a bandgap–implied voltage offset $E_g/q–iV_{oc}$ of approximatively 550 mV.

Contrary to the earlier version of the tool where the bias light intensity was controlled manually using neutral-density filters, the bias light intensity is now automatically controlled by directly changing the current input into the LED light source. As a result, Suns–ERE measurements can be performed systematically and rapidly with a high level of precision. An example of a Suns–ERE curve taken on a CdSeTe sample is shown in Figure 21 (Left). A similar curve taken on a c-Si absorber on the older tool is shown on Figure 21 (Right), illustrating the increased accuracy achieved with the new tool.

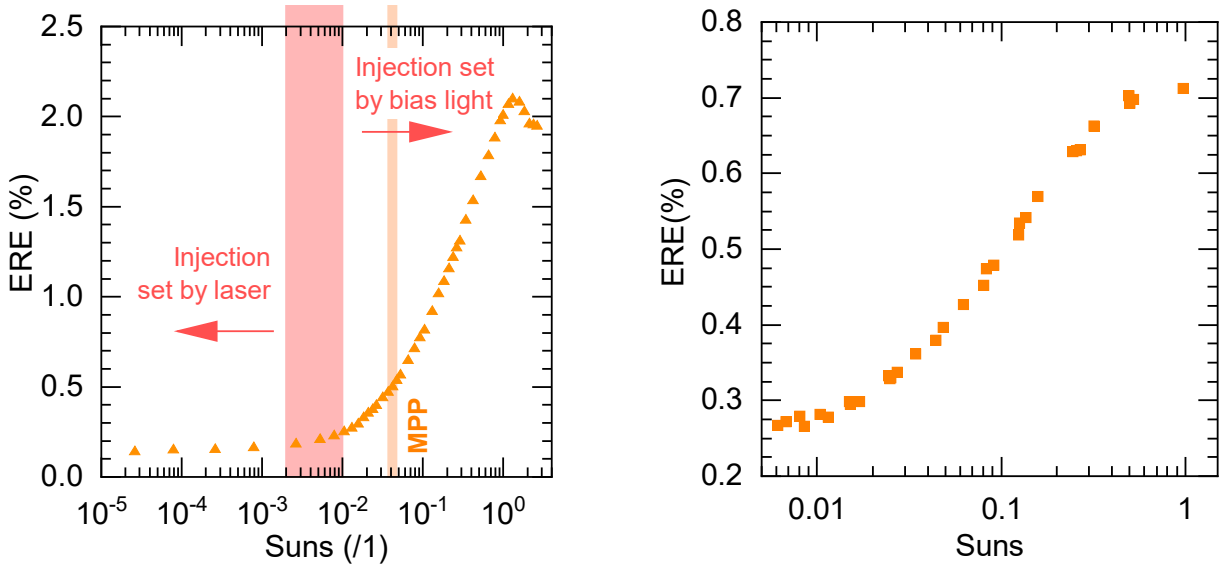

Figure 21. Left: Suns–ERE curve measured on a CdSeTe absorber with the newer version of the tool, with the different regions of injection shown. Right: Suns–ERE curve measured on an c-Si absorber using the original tool, with reduced accuracy.

At lower bias light intensity (<0.01 suns equivalent, left of the region highlighted in red in Figure 21) the injection is set by the comparatively higher power excitation laser and the number of suns equivalent becomes unreliable. However, this level of injection is far away from the region of interest between the maximum power point (MPP, at approximatively 0.05 suns equivalent, shown in orange in Figure 21) and open-circuit (1 sun equivalent).

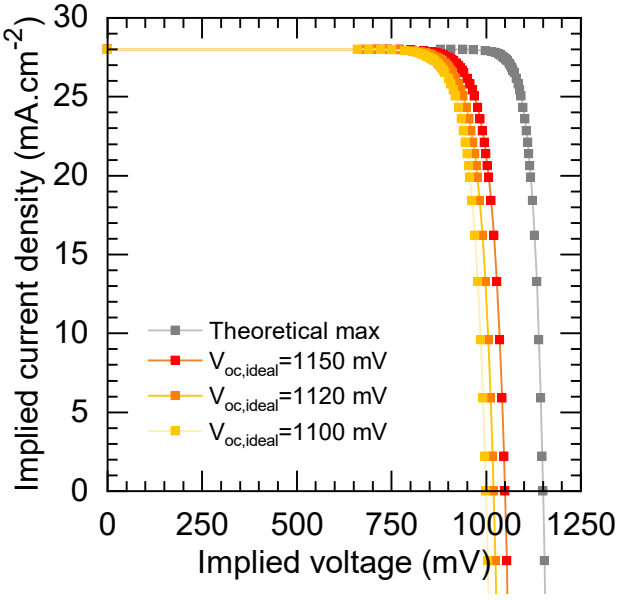

Figure 22. Implied J–V curves under different assumptions for $V_{oc,ideal}$, reconstructed from the Suns–ERE measurement shown in Figure 21 (Left), taken on a CdSeTe absorber. The gray curve corresponds to the theoretical maximal J–V curve obtainable when $V_{oc,ideal}$=1150 mV and ERE=1 at all injection levels.

From Suns–ERE measurements such as the one shown in Figure 21 (Left), the implied *J–V* curve can be reconstructed knowing the thermodynamic voltage limit $V_{oc,ideal}$ for the sample in question. For each injection level (*i.e.*, suns equivalent *X*), the implied voltage *iV* is given by:

$$iV^{X\ suns} = V_{oc,ideal}^{1\ sun} + \left(\frac{k_B T}{q}\right)\ln(X) + \left(\frac{k_B T}{q}\right)\ln(ERE^{X\ suns}).$$

The corresponding implied current density *iJ* is then obtained from the superposition principle:

$$iJ^{X\ suns} = J_{sc}(1 - X).$$

The implied *J–V* curve is then reconstructed by mapping the *iJ–iV* pairs obtained for each injection level *X*. Such an example in shown in Figure 22 from the Suns–ERE curve shown in Figure 21 (Left). $V_{oc,ideal}$ has not yet been calculated accurately for the sample in question. As a result, we show 3 implied *J–V* curves corresponding to 3 assumptions for $V_{oc,ideal}$.

The Suns–ERE tool was subsequently fully automated to make injection-dependent *ERE* measurements both fast and accessible to non-expert users. As shown in Figure 23, the automation script, written in Python, controls the bias light source and the X, Y, and Z position of the sample. The locked-in photoluminescence signal is pulled from the lock-in amplifier—the sensitivity of which is also controlled through the Python script—along with the signal from the illumination-monitoring photodetector. Calculations of the suns equivalent and of the *ERE*, and reconstruction of the implied *J–V* curve, are all performed through the Python script. Once the script is started, the entire operation of the tool is done through a *tkinter* user interface, with no interaction with the Python code required.

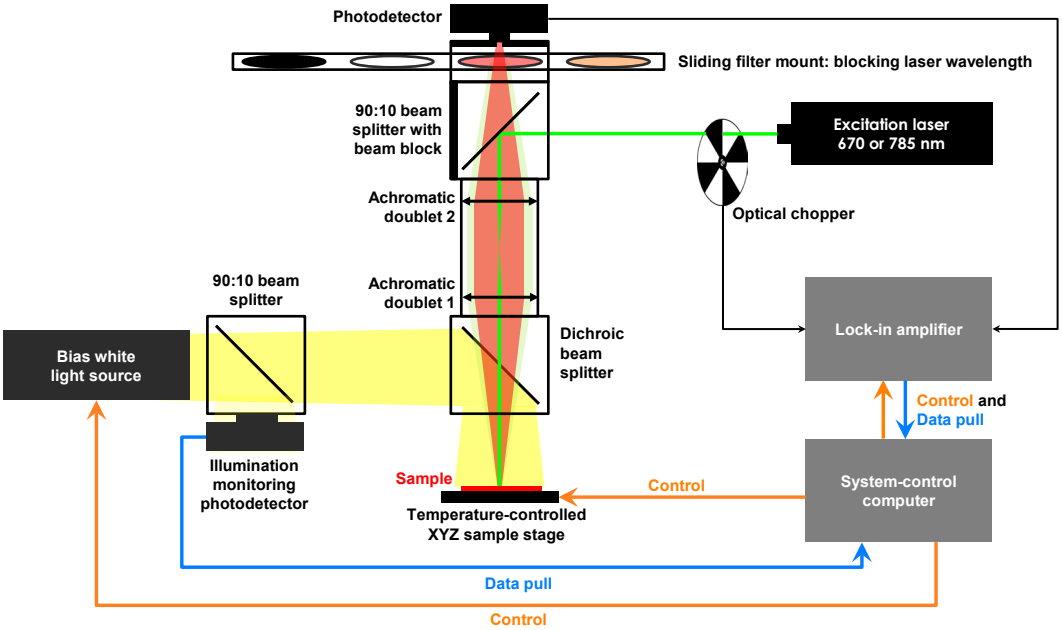

Figure 23. Schematic of the new Suns–ERE tool, showing the control and data pull from and to the computer.

On top of allowing rapid automatic measurement of Suns–ERE curves, our automation script makes it possible to generate ERE maps at a fixed injection level—1-sun-equivalent for open-circuit conditions and approximately 0.05-sun-equivalent for maximum-power-point conditions—by rastering the measurement across the sample. Examples are shown in Figure 24 for crystalline silicon and CdSeTe samples. The system currently operates with a 2-mm resolution (*i.e.*, each pixel corresponds to a 2×2 mm area), although the resolution could easily be reduced to 1 mm. The acquisition time for each pixel is approximately 5 seconds, meaning that a 20×20 mm map takes about 10 minutes to acquire.

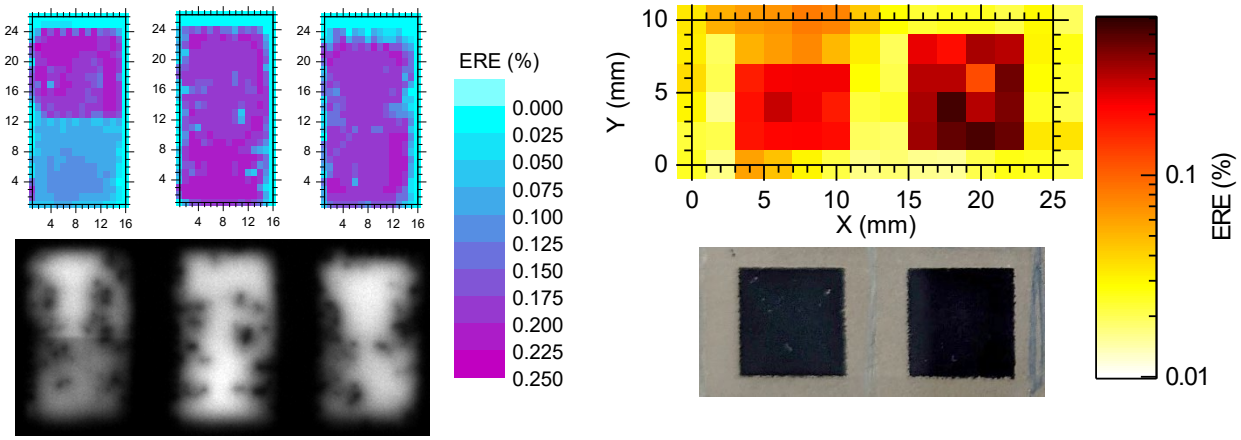

Figure 24. ***Left****. Comparison between ERE maps (top) and non-calibrated photoluminescence (PL) images (bottom) taken on crystalline silicon samples with different metallization schemes. The scales on the X and Y axes are in millimeters. The features due to the metallization and to local defects match between the two techniques. Importantly, the non-calibrated PL imaging is not quantitative whereas the ERE map is quantitative.* ***Right****. ERE map of a high-ERE (>0.1%) CdSeTe sample (top). Two delineated devices are visible, as shown in the sample picture (bottom).*

Among the thin-film solar cell manufacturers we partner with, two US companies for which we have performed *ERE* measurements have asked us to build replicas of the tool for their in-house operations. Two simplified copies of the tool—with only one excitation laser, no mapping capabilities, and no temperature control of the sample—were assembled and delivered to these industry partners. The total cost of these systems (covered by the companies) was below $20,000 each, and they were mostly built from off-the-shelf components from scientific equipment manufacturers (*e.g.*, Thorlabs, Semrock). We also trained the future tool owners on the operation of the tool, both manually and through our automated script. We also shared the list of parts and our Python code with an academic partner (Drexel University) who will build their own tool. We plan to make our Python code publicly available (through GitHub) along with the list of parts and detailed instruction for any team to build their own replica of the tool.

Milestone 1.2.6: No metastability observed during Suns–ERE measurements on CdSeTe devices (Q6)

Comparisons between Suns–ERE curves acquired automatically using our Python script and manually are shown in Figure 25. Two samples are shown: a “good” sample, with an *ERE* between 0.01% and 0.2% and an “excellent” sample with an *ERE* above 2%. Note that the manual and automatic measurements were performed on different locations of the sample on different days. Consequently, the observed difference is expected and is within the usual deviation observed within samples. These results validate our tool automation technique. Each of the automatically acquired Suns–ERE curves displayed in Figure 25 is comprised of 100 data points, with an acquisition time of 2 second per data point, leading to a total measurement time of less than 3 minutes per sample. In comparison, the manual measurements take between 20 and 30 minutes for less than half the number of data points.

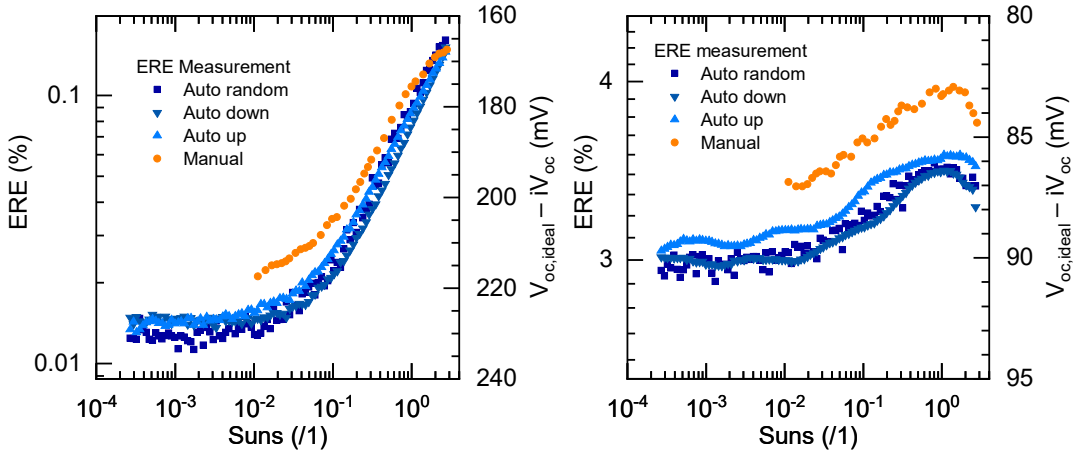

Figure 25. Suns–ERE curves measured on a “good” (left) and on an “excellent” (right) CdSeTe sample. The blue data points correspond to measurements performed automatically, either with increasing, decreasing, or randomly changing the injection level at each step (by controlling the illumination of the samples through the white-LED bias light). The orange data points correspond to manual measurements. Manual measurements were performed on a different day and not on the exact same locations on the devices, hence the difference between the automatically and manually acquired ERE curves.

A concern with injection-dependent measurements is the potential triggering of meta-stability of the sample during the measurement. Such metastable behavior has been documented in CdTe-based solar cells [30]. To verify whether this phenomenon was occurring during our measurements of CdSeTe solar cells fabricated at Colorado State University, we performed automated measurements, sweeping the injection from low to high (upward-pointing triangles in Figure 25), from high to low (downward-pointing triangles), or randomly (squares). The three curves match closely, demonstrating that, even if metastability is present, it is negligible. The reason of the slight difference between the three curves is currently unknown. This behavior could be caused by either:

- A minor metastability of the samples,
- A delay in the temperature increase/decrease of the sample after a change in illumination, or

- A too short time between measurements, with the lock-in amplifier not having enough time to stabilize.

Milestone 1.2.7: Resistance accounting on Cd(Se)Te devices (Q8)

This milestone was gated by successful TLM measurements, which, per Milestone 1.2.4, were not able to be made successfully on CdSeTe devices.

Milestone 1.2.8: Journal publication detailing the characterization platform and loss analysis of Cd(Se)Te (Q8)

Our team published many papers in this project—detailed in the Products section below—but the paper that most comprehensively described the characterization platform and loss analysis in CdSeTe solar cells is Arthur Onno; Carey Reich; Siming Li; Adam Danielson; William Weigand; Alexandra Bothwell; Sachit Grover; Jeff Bailey; Gang Xiong; Darius Kuciauskas; Walajabad Sampath; Zachary C. Holman, Understanding what limits the voltage of polycrystalline CdSeTe solar cells, *Nature Energy*, 2022.

Sub-task 1.3: Extension of the characterization platform to other absorber materials, including perovskites

Milestone 1.3.2: Refractive index of perovskite (n, k) accurately determined (Q9)

We used multi-angle spectroscopic ellipsometry and spectrophotometry to uniquely determine the optical constants of two specific compositions of CsBr perovskite with bandgaps of approximately 1.63 (Cs17/Br17, the composition used in excellent perovskite/silicon and perovskite/perovskite tandem) and 1.68 eV (Cs25/Br20). These bandgaps are achieved by varying the Cs/FA ratio by changing the relative concentration of CsI to PbI_2, and by varying the Br/I ratio by changing the relative concentration of FAI to FABr in the precurser solution. We first verified our methodology on a more commonly used absorber, $CH_3NH_3PbI_3$ (MAPI), that has a bandgap of 1.57 eV and for which reference optical constants are available in the literature. After applying the same methodology to the CsBr perovskites, we simulated the absorptance and reflectance of single-junction perovskite cells with the obtained refractive indices, and compared the results to the measured spectra.

Figure 26 shows the measured ellipsometric, transmittance, and reflectance spectra for one of the perovskite compositions (CS25/BR20), as well as the fits to those spectra that were used to determine the complex refractive index.

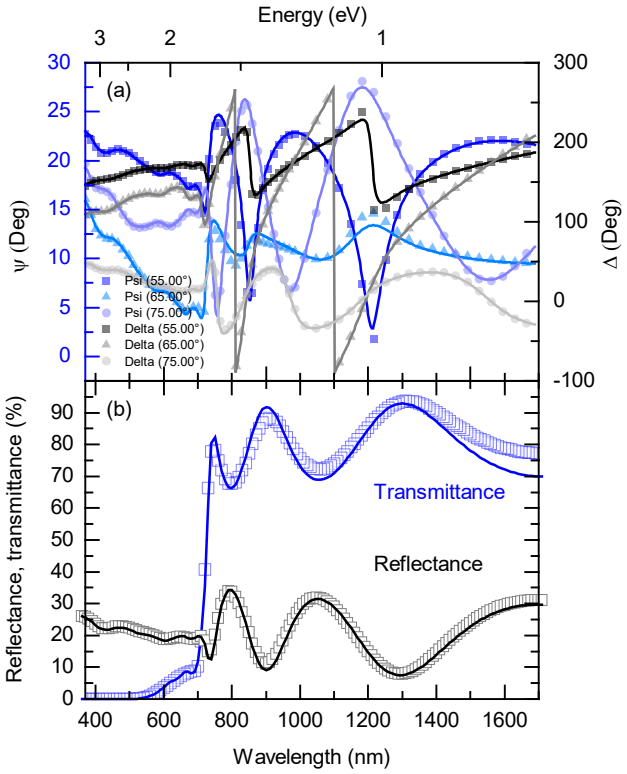

Figure 26. Simulated (line) and measured (symbol) (a) multi-angle spectroscopic ellipsometry spectra and (b) reflectance and transmittance spectra of a Cs25/Br20 film on quartz.

The refractive indices determined from this fitting procedure are shown in Figure 27 for all three perovskite compositions investigated. Note the increasing bandgap with increasing Cs and Br content, manifested as a redshift in the refractive index "peaks" that arise from energy transitions.

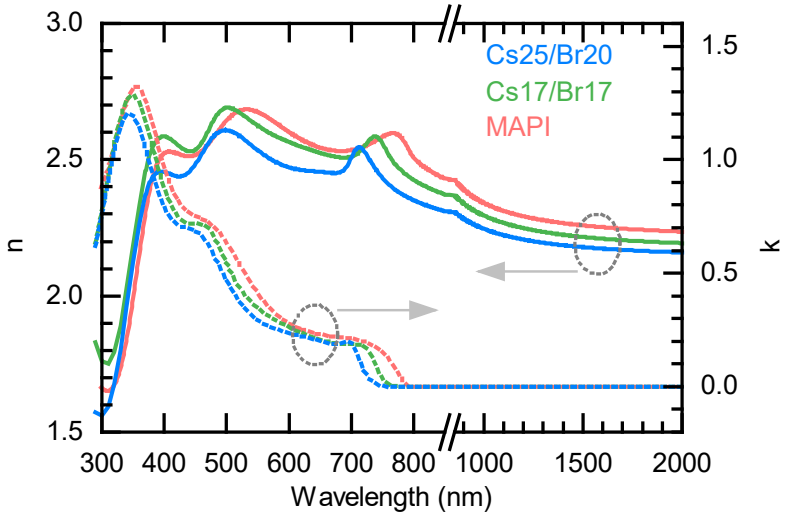

Figure 27. Optical constants of Cs25/Br20, Cs17/Br17, and MAPI perovskites as determined from fitting ellipsometry and spectrophotometry data.

Figure 28 compares the simulated and measured EQE and reflectance (plotted as 1–reflectance) of Cs25/Br20 and Cs17/Br17 perovskite solar cells. The simulations used the complex refractive indices from the previous figure for the perovskite absorber layers, and similarly determined refractive indices for the contact and electrode layers. The simulated EQE is actually the calculated absorptance in the perovskite film, which is equivalent to EQE for a carrier collection efficiency of unity, which is a good assumption at short circuit for high-efficiency solar cells. Figure 28 shows very good agreement between the measured and simulated data, giving us high confidence in the constituent refractive indices.

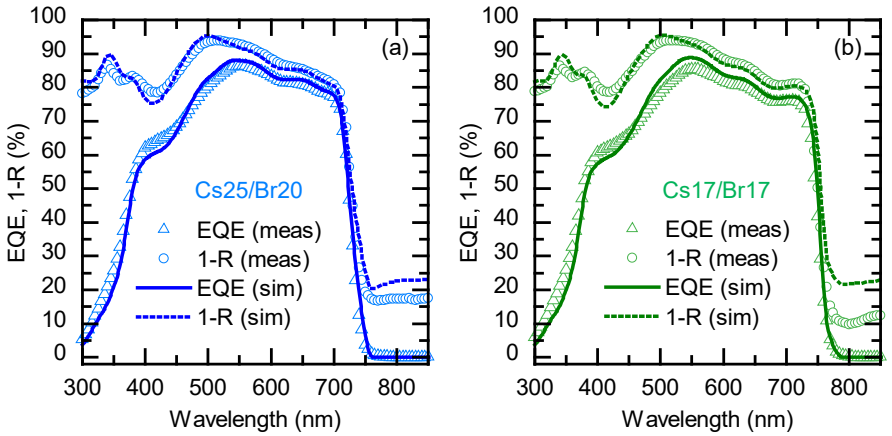

Figure 28. Simulated (line) and measured (symbol) total absorptance (1-R) and EQE of (a) Cs25/Br20 and (b) Cs17/Br17 cells with detached silver reflectors.

Milestone 1.3.3: Determination of the iV_{oc} on perovskite absorbers and devices using ERE at one sun (Q10)

The ERE technique has been successfully used on perovskite test structures and finished devices. As shown in Figure 29, comparison between the ERE-derived iV_{oc} and the terminal voltage V_{oc} has been used to assess the passivation and the selectivity of a range of common contact structures to wide-bandgap (1.7 eV) perovskite absorbers.

For the samples incorporating both an electron transport layer and a hole transport layer, the measurements were repeatable with no statistically significant difference in the results, even after more than a month of storage between measurements (the samples were stored in the dark under nitrogen atmosphere between measurements). Samples where the perovskite absorber was in direct contact with air exhibited an increase in ERE, a known phenomenon due to phase-segregation of the perovskite [31]. Samples where the perovskite absorber was in direct contact with the Au or Ag electrode exhibited a rapid decrease in ERE, also a known phenomenon due to degradation of the perovskite material when in contact with metal electrodes [32]. A paper describing this study was published in *Solar RRL*.

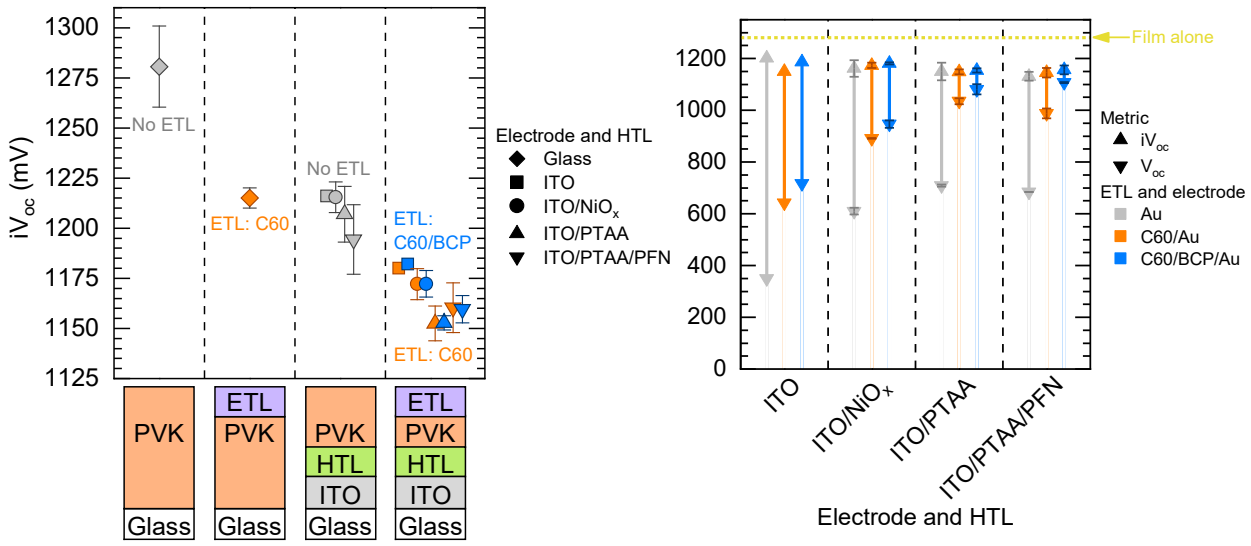

Figure 29. Left: iV_{oc}, derived from ERE measurements, for a range of test structures and finished devices. Right: comparison between iV_{oc} and V_{oc} for finished devices with 12 combinations of contact structures (3 types of electron contacts, 4 types of hole contacts), showing the breakdown of voltage losses between non-radiative recombination and selectivity losses.

Milestone 1.3.4: Reconstruction of the implied J–V curve of perovskite devices (Q11)

After the injection-dependent Suns–ERE measurements were fully automated, such measurements were routinely performed on perovskite devices fabricated by our team to diagnose the sources of recombination and to improve the selectivity of contacts. An example of a comparison between a reconstructed implied *J–V* curve and an actual electrically measured *J–V* curve is shown in Figure 30. These measurements reveal that this particular sample has a prominent iV_{oc}–V_{oc} loss, indicating imperfect selectivity of at least one of the contacts.

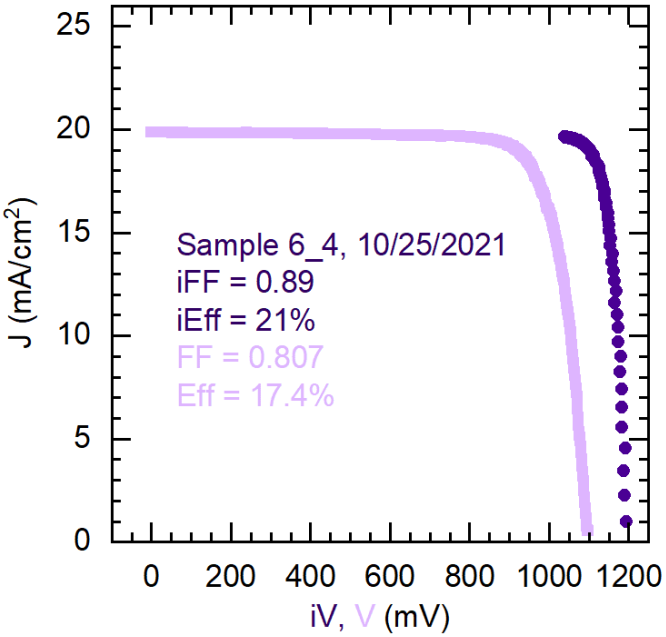

Figure 30. Example of a comparison between the implied (dark purple) and the actual (light purple) J–V curves for a wide-bandgap (approximately 1.67 eV) metal halide perovskite solar cell. Beyond comparison between V_{oc} and iV_{oc}, comparisons between the implied and the actual FF and between the implied and the actual efficiency are possible.

Milestone 1.3.5: No metastability observed during Suns–ERE measurements on perovskite devices (Q11)

We were only able to briefly study this issue. We found that measurements were reproducible with no metastability observed on finished perovskite devices (with both hole and electron contacts) fabricated by partners at University of Colorado/NREL. On the other hand, samples for which the perovskite layer is in direct contact with air can show degradation, with phase segregation leading to "photo-brightening" [31]. To study these phenomena in detail, it would be helpful to add a time-dependent measurement mode in our automated Python script.

Milestone 1.3.6: Resistance accounting on perovskite devices (Q12)

This milestone was gated by successful TLM measurements, which, as on CdSeTe devices (Milestone 1.2.4), were not able to be made successfully on perovskite devices.

Milestone 1.3.7: Journal publication detailing loss analysis of perovskite devices (Q12)

A manuscript on voltage losses in wide-bandgap perovskite solar cells using a range of common electron and hole transport layer was published as Shalinee Kavadiya; Arthur Onno; Caleb Boyd; Xingyi Wang; Alexa Cetta; Michael McGehee; Zachary Holman, Investigation of the Selectivity of Carrier Transport Layers in Wide-Bandgap Perovskite Solar Cells, *Solar RRL*, 2021

Task 2: 24%-efficient CdSeTe solar cells through novel selective contacts and comprehensive loss analysis

Sub-task 2.1: Development of advanced passivation layers for CdSeTe, leading to iV_{oc}>1 V

Milestone 2.1.1: Cd(Se)Te absorber with a lifetime >100 ns and a $N_a > 10^{15}$ cm^{-3} (Q6)

Early tests with group V (As) doping of CdSeTe absorbers led to the achievement of this milestone, as shown on the time-resolved photoluminescence (TRPL) and the C-V measurements displayed in Figure 31, with a lifetime of 117 ns and a minimum carrier concentration of 1.25×10^{15} cm^{-3}. This result was obtained on a CdSeTe/CdTe/CdSeTe structure with a Te back contact, without needing an Al_2O_3 passivation layer.

Using scanning capacitance microscopy, this high majority carrier concentration has been confirmed at the *front* of the device, in the vicinity of the MZO/CdSeTe heterojunction. Deeper into the absorber, a majority carrier concentration of 10^{18} cm^{-3} was extracted from the same scanning capacitance microscopy measurement. These results are in line with the As doping concentration

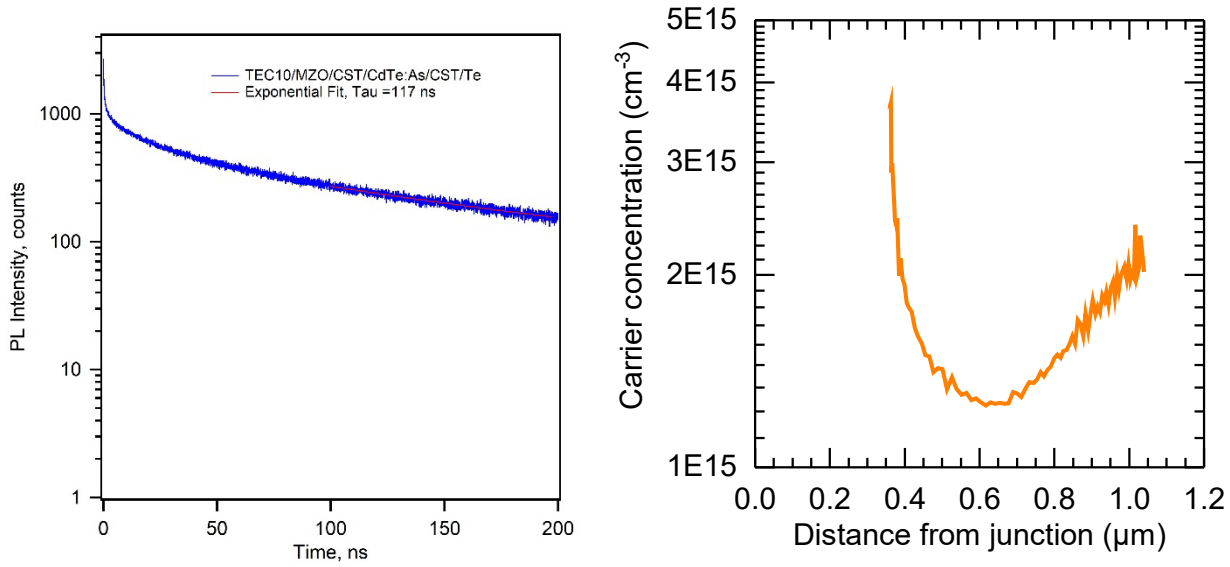

Figure 31. Left: TRPL measurement of the CdSeTe/CdTe:As/CdSeTe, showing a lifetime of 117 ns. Right: C-V measurement, showing an acceptor density above 1.25×10^{15} cm^{-3}.

Milestone 2.1.2: CdSeTe absorber with iV_{oc}>1 V (Q5)

Samples were fabricated using the conventional CdSeTe/CdTe bilayer approach as well as using full CdSeTe (no CdTe) absorbers. Aluminum oxide (Al_2O_3) passivation layers were then deposited by either sputtering or atomic layer deposition (ALD). The results in term of $V_{oc,ideal}$ and iV_{oc} for this set of sample are shown in Figure 32.

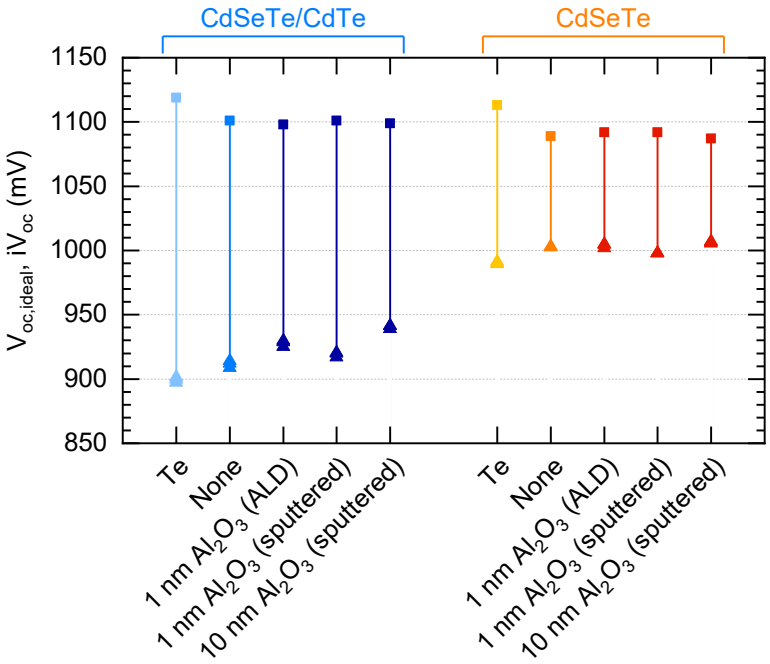

Figure 32. $V_{oc,ideal}$ (rectangle) and iV_{oc} (upward-pointing triangles) for samples fabricated with a conventional CdSeTe/CdTe bilayer absorber (blue) or with a full CdSeTe absorber (orange/red) and different flavors of passivating layers at the back of the device (x-axis labels). For each sample, the length of the line connecting the two data points quantifies the voltage losses due to non-radiative recombination.

For the samples fabricated with a CdSeTe/CdTe bilayer, the *ERE* is below 0.2%, in line with previous experiments. However, for the full-CdSeTe absorbers, excellent *ERE* results (>2.5%) were obtained for samples with an Al_2O_3-based passivated back contact. Thus, despite sizable sub-bandgap features—which reduce the theoretical voltage limit $V_{oc,ideal}$ below 1100 V—these devices exhibit iV_{oc} values in excess of 1 V. Milestone 2.1.2 is, thus, met. These results are further corroborated by time-resolved photoluminescence (TRPL) measurements, shown in Figure 33. Lifetimes between 4 and 7 µs are obtained when fitting the tail of the TRPL decay.

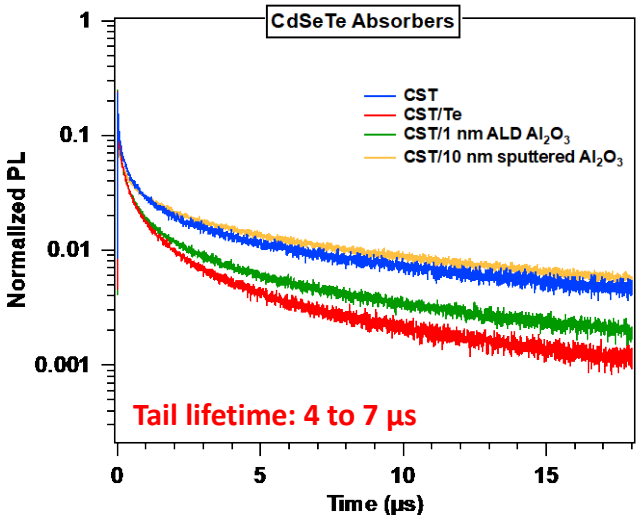

Figure 33. TRPL data for a subset of the samples shown in Figure 32. Tail lifetimes in excess of 4 µs were extracted from these measurements.

Strikingly, the samples with no passivation layer and no back contact (marked as "None" in Figure 32) exhibit *ERE* values as high as samples with Al_2O_3 passivation layers. We attribute this behavior to the growth of a native passivating oxide layer at the back of the device. Moreover, for both CdSeTe and CdSeTe/CdTe absorbers, samples with 10 nm of Al_2O_3 deposited by ALD, not shown here, had *ERE* values below the detection limit of the *ERE* tool (unlike the samples with 1-nm-thick ALD Al_2O_3 layers). We attribute this behavior to the highly compact and conformal nature of Al_2O_3 deposited by ALD, as opposed to more porous, less conformal sputter-deposited Al_2O_3. We hypothesize that the chlorination process performed *after* Al_2O_3 ALD deposition was blocked by this thick compact conformal layer, with no activation of the CdSeTe film.

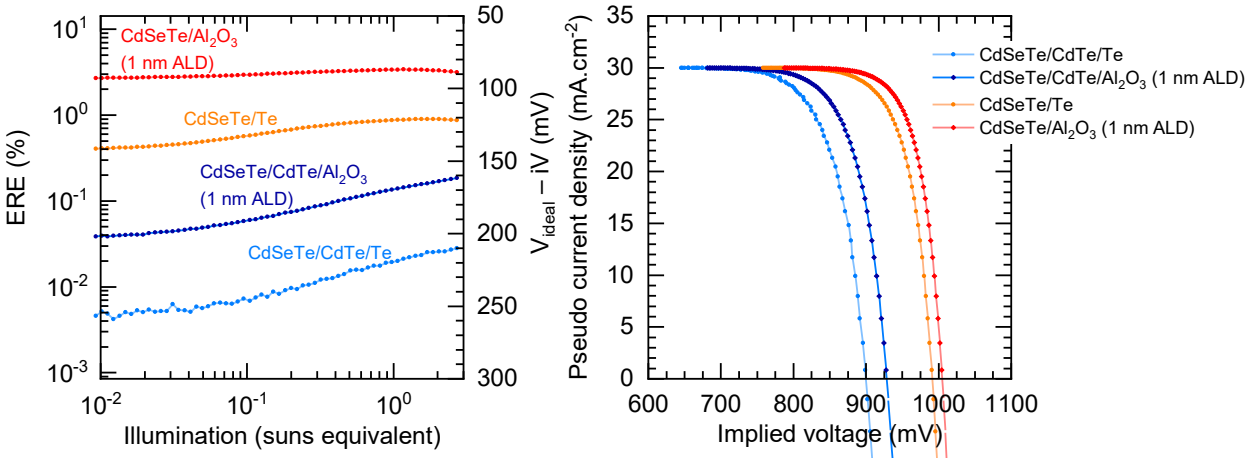

*Figure 34. **Left**. Suns–ERE curves for a subset of the samples shown in Figure 32. Samples based on CdSeTe/CdTe absorbers are in blue, samples based on a full-CdSeTe absorbers are in orange/red. **Right**. Reconstructed J–V curves from the Suns–ERE data.*

The Suns–ERE and associated reconstructed implied *J–V* curves for a subset of samples are shown in Figure 34. Notably, the shape of the Suns–ERE curve is correlated with the absolute *ERE* value at 1 sun-equivalent. The best samples (full CdSeTe absorbers with passivated with Al_2O_3) exhibit a relatively constant *ERE* across the range of injection tested, whereas lower-*ERE* samples exhibit an increase in *ERE* by a half order of magnitude with injection. We associate this with the type of dominant recombination in each sample: radiative recombination, which is mostly injection-independent, dominate in passivated full CdSeTe absorbers; non-radiative recombination, which is generally highly injection-dependent, dominates in CdSeTe/CdTe absorbers.

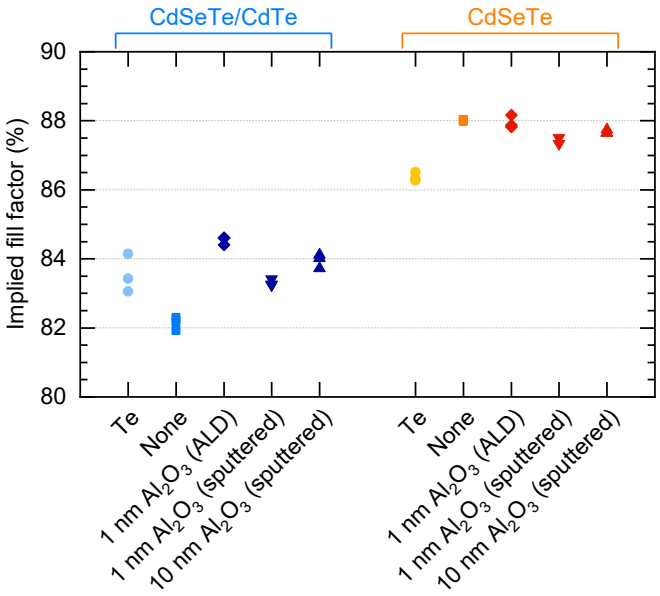

Figure 35. Implied fill factors for the samples shown in Figure 32.

As a result, the implied FF, shown in Figure 35, is higher for full CdSeTe absorbers. Hence, the implied efficiency–calculated with the assumption of a 30 mA.cm^{-2} short-circuit current density J_{sc}—exceeds 26% for the full CdSeTe samples, as shown in Figure 36.

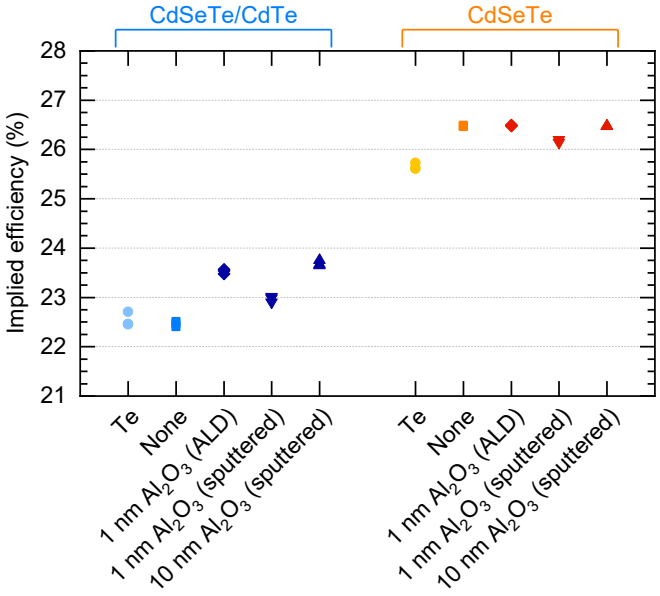

Figure 36. Implied efficiencies for the samples shown in Figure 32.

Milestone 2.1.3: iV_{oc}>1 V on Cd(Se)Te with passivation layers suitable for charge carrier extraction (Q6)

Contact layers that are *both* highly passivating (high iV_{oc}) and yet conductive to one carrier type (selective—enabling low contact resistivity) proved to be extremely challenging. Obtaining one or the other property was possible with many contact layers; obtaining both was not possible with any of the layers measured in this project.

Milestone 2.2.1: Selective contact ($iV_{oc} - V_{oc} < 0.1$ V) on CdSeTe (Q6)

The full voltage loss analysis for a set of six characteristic sample plates—three Cu-doped, three As-doped—is displayed in Figure 37. The leftmost sample plate is a high-voltage (860–875 mV) high-efficiency (>20%) Cu-doped sample with a baseline Te back contact, among the best plate of devices made at Colorado State University. Because of the differences in sub-bandgap behaviors previously discussed, As-doped devices exhibit a reduction of $V_{oc,ideal}$ and this reduction of $V_{oc,ideal}$ is exacerbated in the presence of a reflective passivating back contact, reaching 65–75 mV in the worst case presented here. Nevertheless, the superior luminescence achieved when combining As-doping with passivating back contacts more than offsets these losses. As a result, we demonstrate iV_{oc} values exceeding 970 mV, more than 80 mV higher than the V_{oc} of the record-efficiency CdSeTe solar cell. The best Cu-doped sample reported here (leftmost data points in Figure 37) also exhibits relatively high iV_{oc} (920–950 mV), tens of millivolts above record-efficiency devices.

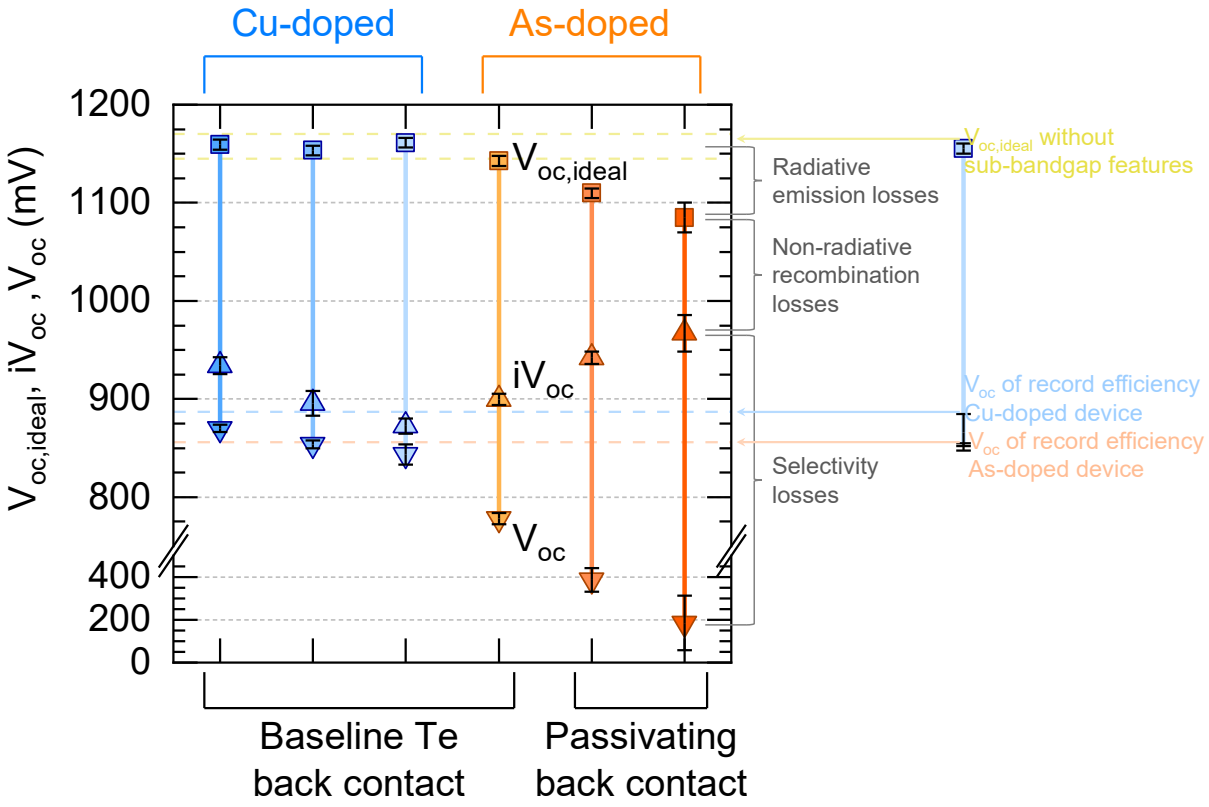

Figure 37. Voltage loss analysis on a subset of six characteristic As-doped and Cu-doped CdSeTe samples using baseline Te and passivating back contacts. The range of $V_{oc,ideal}$ obtained in the absence of sub-bandgap features for 1.41–1.44 eV CdSeTe absorbers is indicated, as well as the V_{oc} of record efficiency As-doped and Cu-doped CdSeTe solar cells.

Notably, all the devices reported here exhibit non-negligible selectivity losses, ranging from 30–65 mV for conventional Cu-doped devices with a baseline Te back contact to several hundreds of millivolts for As-doped devices with a passivating back contact. Beyond the six samples reported in Figure 37, we have not encountered any sample for

which V_{oc} matched iV_{oc}. This is somewhat striking, as V_{oc} closely matches iV_{oc} under 1-sun illumination for mature crystalline silicon solar cell technologies [33,34], and similar V_{oc}–iV_{oc} matching has recently been demonstrated with perovskite solar cells [11]. The assumption that V_{oc}=iV_{oc} in CdSeTe solar cells is, thus, generally wrong.

Among Cu-doped devices—all three of them fabricated with a baseline Te back contact—the 20%-efficient sample exhibits the highest iV_{oc} but also the highest selectivity losses (approximatively 65 mV, S_{oc}=0.93), which is unexpected given that a poor selectivity stems from a combination of poor passivation and poor conductivity [35]. This sample appears to strike a balance between passivation and conductivity to achieve a comparatively high efficiency without overly sacrificing its V_{oc} nor its fill factor. The two other Cu-doped samples demonstrate an example where V_{oc} is approximatively the same (within 10 mV with overlap of the distributions) but iV_{oc} differs appreciably (>20 mV, no overlap between the distributions). Thus, these samples achieve a similar V_{oc} for different reasons: the first one exhibits lower non-radiative recombination (*i.e.*, higher *ERE*), the second one achieves higher selectivity.

In order to investigate the interplay between As doping and selectivity, samples with increasing amount of As were provided by First Solar (the As doping level cannot be easily varied in samples fabricated at Colorado State University). As shown in Figure 38, similar to the samples fabricated as Colorado State University, the extent of sub-bandgap features increases with increasing As doping in both stand-alone films and finished devices. Note that, for a given level of As, films and devices were fabricated together and the processing associated with deposition of the back contact is the only difference between the films and the devices.

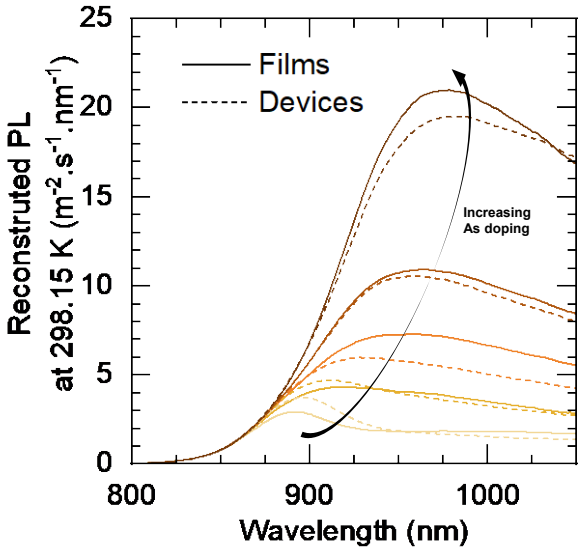

Figure 38. Reconstructed PL emission at 298.15 K for films and devices fabricated at First Solar with increasing As content.

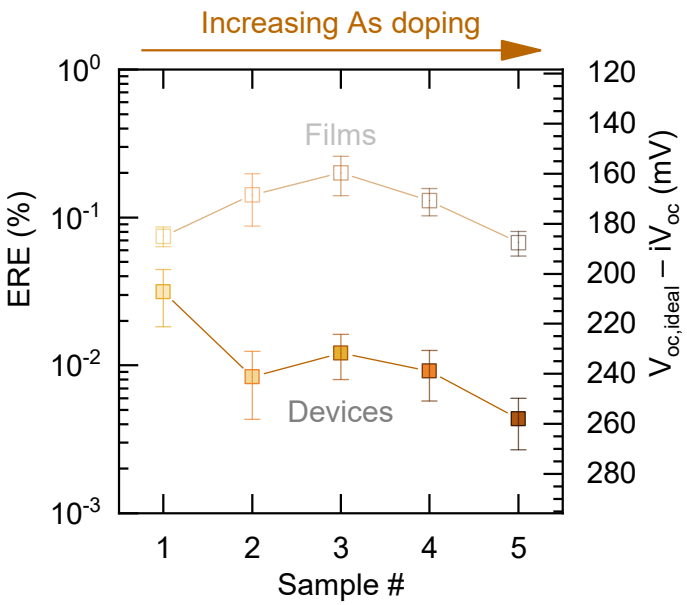

Figure 39. ERE for films and devices fabricated at First Solar with increasing As content.

The *ERE*, on the other hand, does not exhibit a monotonic variation with increasing As doping, as shown in Figure 39: the *ERE* increases and then decreases with the increasing As doping. We attribute the increase at low As doping to the associated increase in acceptor concentration—as the quasi-Fermi level of holes is fixed by the acceptor concentration in these devices operating in low injection—and the decrease at high As doping to the increase in As-related defects states and the increased carrier compensation as the activation ratio of dopant atoms decreases.

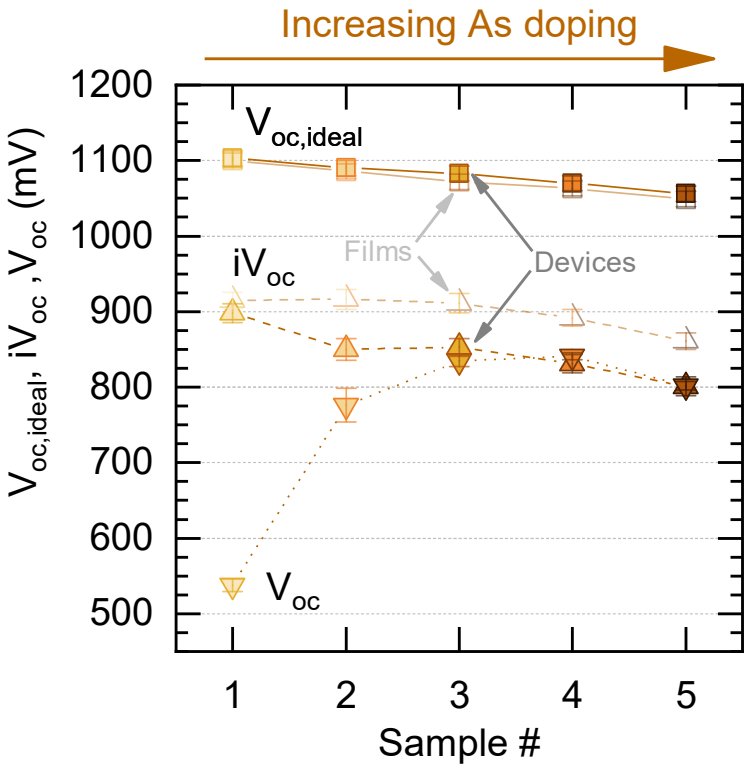

Figure 40. Voltage loss analysis for finished devices and for films with a free back surface fabricated by First Solar with increasing As doping.

As shown in Figure 40, due to the combined reduction of $V_{oc,ideal}$—due to increased sub-bandgap features with increasing As content—and of *ERE* at high As concentration, the iV_{oc} of both films and devices plateaus before decreasing with increasing As doping. Two crucial results appear in Figure 40. First, iV_{oc} drops by approximately 60 mV upon deposition of the back contact (apart for the sample with the lowest As concentration). This is either due to a poor passivation of the back contact or to a degradation of the absorber during the back-contact deposition process.

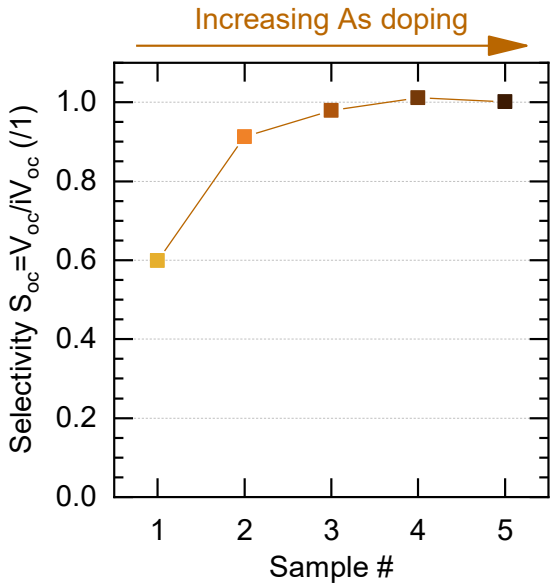

Figure 41. Selectivity metric $S_{oc}=V_{oc}/iV_{oc}$ for the samples fabricated by First Solar.

Second, as shown in Figure 41, the selectivity improves steadily with As incorporation, with S_{oc} reaching unity ($V_{oc}=iV_{oc}$) when the As doping is high enough. This result is expected: the higher hole concentration and lower electron concentration at the back of the absorber leads to a high ratio of conductivities between holes and electrons and, thus, to a high selectivity. This demonstrates that, when combined with an appropriate contact (nitrogen-doped ZnTe in the case of the devices fabricated at First Solar) proper absorber engineering can help drive carrier selectivity.

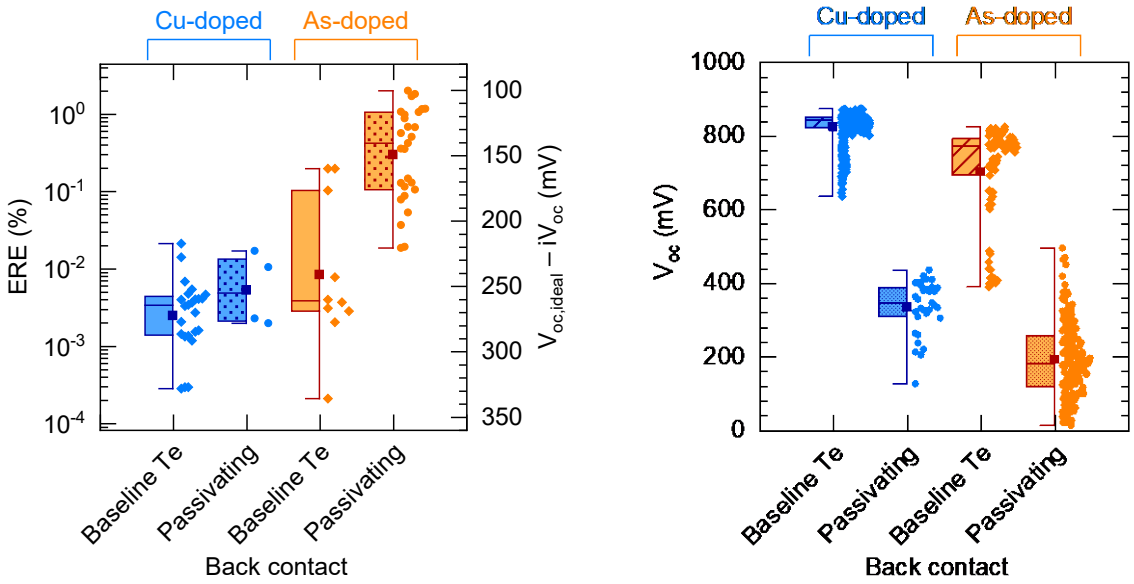

*Figure 42. Statistical analysis of the ERE **(left)** and the V_{oc} **(right)** measured on Cu-doped and As-doped devices with baseline Te and passivating Al_2O_3/-aSi:H(p)/ITO/Ag back contacts.*

In comparison, as shown in Figure 42, the Al_2O_3/a-Si:H(p)/ITO/Ag contacts we have been working on in collaboration between Colorado State University and Arizona State University have proved to be poorly selective despite a good passivation, with high *ERE* values but low voltages.

Milestones 2.2.2, 2.3.1, 2.3.2, 2.3.3, 2.4.1, 2.4.2, and 2.4.3:

These milestones focused on CdSeTe device performance, including high FF and high efficiency. We were not able to make substantial progress towards meeting these milestones within the timeline of the project; although the characterization platform worked as planned and provided a lot of insight into and understanding about the state of the art contacts used by the community, it did quickly guide the team to better ocntacts.

Significant Accomplishments and Conclusions: This project changed the way the CdTe community thinks about voltage losses and the way that it assesses prospective contacts. It introduced a tool that brought the community information about the voltage that a cell *could* achieve its contacts were perfectly selective, thus enabling disambiguation of recombination and resistive losses. This capability has long been utilized in silicon solar cell development but the same technique doesn't work for thin films; this project created a new technique that achieved the same outcome. This tool then revealed that the bulk of CdSeTe and available passivation layers (e.g., Al_2O_3) are already quite good—good enough for 1 V iV_{oc}—but that no contacts yet exist that allow for this full potential to be extracted as electrical voltage at the cell electrodes. Two US cell manufacturers procured the tool developed in this project, showing the demand for this technique by US industry. Over 10 papers were published based on this work and several excellent students and postdocs were trained.

Path Forward: While the majority of the tasks in this project were highly successful, two were not and are worthy of additional attention. First, vertical TLM measurements have proven challenging on both CdSeTe and perovskite devices—indeed, contact resistivities are *still* no reported in the thin-film solar community because of this difficulty, and we believe that this impedes the community's progress in finding excellent contact materials. We now recommend exploring conventional lateral TLM using photolithography techniques to get to small enough feature sizes that the sheet resistance (through the absorber) is comparable to or less than the contact resistance.

The second task in which this project fell short was the demonstration of high-efficiency CdSeTe cells, and the underlying reason was because a contact that is *both* passivating and carrier selective was not found. We suggest understanding the role of CdTe in the performance of the back hole contact and why directly contacting the CdSeTe absorber leads to poor selectivity. As the presence of recombination-active CdTe reduces iV_{oc}, we will also suggest focusing on alternatives to circumvent its use and to directly contact the high-iV_{oc} CdSeTe material. Toward that goal, we would investigate the performance of alternative combinations of high-work-function semiconductors and metals (*e.g.*, TiO_x, NiO_x, MoO_x, Ni, Pt) as back contact layers. Additionally, using corona-charging with Suns-ERE, it would be possible to characterize the charge and the density of defects at the

$CdTe/Al_2O_3$ and $CdSeTe/Al_2O_3$ interfaces to diagnose whether a detrimental downward band bending occurs at the back of the device.

Products:

M. Mahaffey, A. Onno, C. Reich, A. Danielson, W. Sampath, and Z. Holman, “Measuring the absorber doping concentration of Si, CdSeTe, and perovskite solar cells using injection-dependent quasi-steady-state photoluminescence,” *IEEE J. Photovoltaics* **13**, 800–807 (2023).

A. Bothwell, C. Reich, A. Danielson, A. Onno, Z. Holman, W. Sampath, and D. Kuciauskas, “Charge carrier lifetime determination in graded absorber solar cells using time-resolved photoluminescence simulations and measurements,” *Solar RRL*, 2201029 (2023).

A. Danielson, C. Reich, R. Pandey, A. Munshi, A. Onno, W. Weigand, D. Kuciauskas, S. Li, A. Bothwell, J. Guo, M. Murugeson, J. McCloy, R. Klie, Z. Holman, and W. Sampath, “Electro-optical characterization of arsenic-doped CdSeTe and CdTe solar cell absorbers doped in-situ during close space sublimation,” *Sol. Energy Mater. Sol. Cells* **251**, 112110 (2023).

A. Onno, C. Reich, S. Li, A. Danielson, W. Weigand, A. Bothwell, S. Grover, J. Bailey, G. Xiong, D. Kuciauskas, W. Sampath, and Z. Holman, “Understanding what limits the voltage of polycrystalline CdSeTe solar cells,” *Nature Energy*, **7**, 400–408 (2022).

D. Kuciauskas, S. Li, J. Moseley, D. Albin, C. Lee, A Onno, and Z. Holman, “Voltage loss comparison in CdSe/CdTe solar cells and polycrystalline CdSeTe heterostructures,” *IEEE J. Photovoltaics* **12**, 6–10 (2022).

G. Yeung, C. Reich, A. Onno, A. Bothwell, A. Danielson, Z. Holman, W. Sampath, and C. Wolden, “Robust passivation of CdSeTe based solar cells using reactively sputtered magnesium zinc oxide,” *Sol. Energy Mater. Sol. Cells* **233**, 111388 (2021).

S. Kavadiya, A. Onno, C. Boyd, X. Wang, A. Cetta, M. McGehee, and Z. Holman, “Investigation of the selectivity of carrier transport layers in wide-bandgap perovskite solar cells,” *Solar RRL* **5**, 2100107 (2021).

Mahisha Amarasinghe; David Albin; Darius Kuciauskas; John Moseley; Craig Perkins; Wyatt Metzger, Mechanisms for long carrier lifetime in Cd(Se)Te double heterostructures, *Applied Physics Letter*, 2021

C. Boyd, R. Shallcross, T. Moot, R. Kerner, L. Bertoluzzi, A. Onno, S. Kavadiya, C. Chosy, E. Wolf, J. Werner, J. Raiford, C. de Paula, A. Palmstrom, Z. Yu, J. Berry, S. Bent, Z. Holman, J. Luther, E. Ratcliff, N. Armstrong, and M. McGehee, “Overcoming redox reactions at perovskite-nickel oxide interfaces to boost voltages in perovskite solar cells,” *Joule* **4**, 1–17 (2020).

Darius Kuciauskas; John Moseley; Patrik Ščajev; David Albin, Radiative Efficiency and Charge-Carrier Lifetimes and Diffusion Length in Polycrystalline CdSeTe Heterostructures, *Physica Status Solidi-Rapid Research Letters*, 2020

Marco Nardone; M Spehar; Darius Kuciauskas; David Albin, Numerical simulation of high-efficiency, scalable, all-back-contact Cd(Se,Te) solar cells, *Journal of Applied Physics*, 2020

A. Onno, C. Chen, P. Koswatta, M. Boccard, and Z. Holman, "Passivation, conductivity, and selectivity in solar cell contacts: concepts and simulations based on a unified partial-resistances framework," *J. Appl. Phys.* **126**, 183103 (2019).

Project Team and Roles:

- Arthur Onno, assistant research professor, Arizona State University: management of the characterization platform development, design of the test experiments, improvements to the ERE setup to make it injection-dependent, reporting to DOE
- Mason Mahaffey, PhD Student, Arizona State University: building and automation of the Suns–ERE tool, ERE measurements
- Darius Kuciauskas, researcher V, NREL: building of an ERE system at NREL in order to test future improvements, interpretation of TRPL and steady-state PL data
- Alexandra Bothwell, postdoctoral research fellow, NREL: building of an ERE system at NREL in order to test future improvements, TRPL and steady-state PL measurement
- Siming Li, postdoctoral research fellow, NREL: building of an ERE system at NREL in order to test future improvements, TRPL and steady-state PL measurement
- Adam Danielson, PhD student, Colorado State University: fabrication of CdSeTe test samples and devices, in particular deposition of the CdSeTe absorbers
- Carey Reich, PhD student, Colorado State University and NREL: TRPL measurements, adaptation of the J_{sc}-V_{oc} method to Cd(Se)Te devices, fabrication of CdSeTe test samples and devices, in particular device post-processing (delineation and metallization)
- Ramesh Pandey, PhD Student, Colorado State University: EQE measurements and CdSeTe device simulations
- Anna Kindvall, Master Student, Colorado State University (Graduated Fall 2019): fabrication of CdSeTe test samples and devices, in particular sputtering of the MZO electron contact and Al_2O_3 passivation layers
- Amit Munshi, research scientist, Colorado State University: operation and maintenance of the Cd(Se)Te solar cells deposition tool
- William Weigand, PhD student, Arizona State University: operation of the a-Si:H PECVD tool, fabrication and measurement of the vertical TLM test samples and compilation of results.
- Salman Manzoor, PhD student, Arizona State University (Graduated Spring 2020): optical characterization (ellipsometry and spectrophotometry) and modeling of CdTe and CdSeTe films

References:

1 A. H. Munshi, J. Kephart, A. Abbas, J. Raguse, J.-N. Beaudry, et al., *IEEE J. Photovolt.* **8,** 310 (2018).

2 T. A. M. Fiducia, B. G. Mendis, K. Li, C. R. M. Grovenor, A. H. Munshi, et al., *Nat. Energy* **4,** 504 (2019).

3 J. M. Kephart, A. Kindvall, D. Williams, D. Kuciauskas, P. Dippo, et al., *IEEE J. Photovolt.* **8,** 587 (2018).

4 M. Amarasinghe, D. Albin, D. Kuciauskas, J. Moseley, C. L. Perkins, et al., *Appl. Phys. Lett.* **118** (2021).

5 D. Kuciauskas, J. M. Kephart, J. Moseley, W. K. Metzger, W. S. Sampath, et al., *Applied Physics Letters* **112** (2018).

6 D. Kuciauskas, D. Albin, J. Moseley, S. Li, P. Ščajev, et al., in *Microsecond Carrier Lifetimes in Polycrystalline CdSeTe Heterostructures and in CdSeTe Thin Film Solar Cells*, Calgary, AB, Canada, 2020, p. 82.

7 B. E. McCandless, W. A. Buchanan, C. P. Thompson, G. Sriramagiri, R. J. Lovelett, et al., *Sci Rep* **8,** 14519 (2018).

8 W. K. Metzger, S. Grover, D. Lu, E. Colegrove, J. Moseley, et al., *Nat. Energy* **4,** 837 (2019).

9 D. Krasikov, D. Guo, S. Demtsu, and I. Sankin, *Sol. Energy Mater. Sol. Cells* **224** (2021).

10 D.-B. Li, C. Yao, S. N. Vijayaraghavan, R. A. Awni, K. K. Subedi, et al., *Nat. Energy* **6,** 715 (2021).

11 Z. Liu, L. Krückemeier, B. Krogmeier, B. Klingebiel, J. A. Márquez, et al., *ACS Energy Lett.* **4,** 110 (2018).

12 B. M. Kayes, H. Nie, R. Twist, S. G. Spruytte, F. Reinhardt, et al., in *27.6% Conversion efficiency, a new record for single-junction solar cells under 1 sun illumination*, Seattle, WA, USA, 2011, p. 4.

13 D. D. Smith, P. Cousins, S. Westerberg, R. De Jesus-Tabajonda, G. Aniero, et al., *IEEE J. Photovolt.* **4,** 1465 (2014).

14 A. Kanevce, M. O. Reese, T. M. Barnes, S. A. Jensen, and W. K. Metzger, *J. Appl. Phys.* **121** (2017).

15 J. N. Duenow, J. M. Burst, D. S. Albin, M. O. Reese, S. A. Jensen, et al., *IEEE J. Photovolt.* **6,** 1641 (2016).

16 A. H. Munshi, C. L. Reich, A. Danielson, R. Pandey, D. Kuciauskas, et al., in *Arsenic Doping of Polycrystalline CdSeTe Devices for Microsecond Life-times with High Carrier Concentrations*, Calgary, AB, Canada, 2020, p. 1824.

17 R. A. Sinton and A. Cuevas, *Appl. Phys. Lett.* **69,** 2510 (1996).

18 A. Cuevas and R. A. Sinton, *Prog. Photovolt. Res. Appl.* **5,** 79 (1997).

19 A. Delamarre, L. Lombez, and J.-F. Guillemoles, *Applied Physics Letters* **100** (2012).

20 J. K. Katahara and H. W. Hillhouse, *J. Appl. Phys.* **116** (2014).

21 V. Sarritzu, N. Sestu, D. Marongiu, X. Chang, S. Masi, et al., *Sci Rep* **7,** 44629 (2017).

22 M. Stolterfoht, P. Caprioglio, C. M. Wolff, J. A. Márquez, J. Nordmann, et al., *Energ Environ Sci* **12,** 2778 (2019).

[23] K. R. McIntosh and S. C. Baker-Finch, in *OPAL 2: Rapid optical simulation of silicon solar cells*, 2012, p. 265.
[24] O. D. Miller, E. Yablonovitch, and S. R. Kurtz, *IEEE J. Photovolt.* **2,** 303 (2012).
[25] F. A. Lindholm, J. G. Fossum, and E. L. Burgess, *IEEE Trans. Electron Devices* **26,** 165 (1979).
[26] S. Manzoor, J. Häusele, K. A. Bush, A. F. Palmstrom, J. Carpenter, et al., *Optics Express* **26,** 27441 (2018).
[27] M. D. Abbott, K. R. McIntosh, and B. Sudbury, in *Optical loss analysis of PV modules*, Munich, Germany, 2016.
[28] R. T. Ross, *J. Chem. Phys.* **46,** 4590 (1967).
[29] P. Würfel, *J. Phys. C* **15,** 3967 (1982).
[30] D. Guo, D. Brinkman, A. R. Shaik, C. Ringhofer, and D. Vasileska, *Journal of Physics D: Applied Physics* **51** (2018).
[31] P. Caprioglio, S. Caicedo-Dávila, T. C.-J. Yang, C. M. Wolff, F. Peña-Camargo, et al., *ACS Energy Lett.* **6,** 419 (2021).
[32] C. C. Boyd, R. Cheacharoen, T. Leijtens, and M. D. McGehee, *Chemical Reviews* **119,** 3418 (2019).
[33] R. Dumbrell, M. K. Juhl, T. Trupke, and Z. Hameiri, *IEEE J. Photovolt.* **7,** 1376 (2017).
[34] M. Bivour, C. Messmer, L. Neusel, F. Zähringer, J. Schön, et al., in *Principles of Carrier-Selective Contacts Based on Induced Junctions*, Amsterdam, The Netherlands, 2017.
[35] A. Onno, C. Chen, P. Koswatta, M. Boccard, and Z. C. Holman, *J. Appl. Phys.* **126,** 183103 (2019).